

Exotic topological point and line nodes in the plaquette excitations of a frustrated Heisenberg antiferromagnet on the honeycomb lattice

Moumita Deb^{1,*} and Asim Kumar Ghosh^{1,†}

¹*Department of Physics, Jadavpur University, 188 Raja Subodh Chandra Mallik Road, Kolkata 700032, India*

A number of topological nodes including Dirac, quadratic and three-band touching points as well as a pair of degenerate Dirac line nodes are found to emerge in the triplet plaquette excitations of the frustrated spin-1/2 J_1 - J_2 antiferromagnetic Heisenberg honeycomb model when the ground state of the system lies in a spin-disordered plaquette-valence-bond-solid phase. A six-spin plaquette operator theory of this honeycomb model has been developed for this purpose by using the eigenstates of an isolated Heisenberg hexagonal plaquette. Spin-1/2 operators are thus expressed in the Fock space spanned by the plaquette operators those are obtained in terms of exact analytic form of eigenstates for a single frustrated Heisenberg hexagon. Ultimately, an effective interacting boson model of this system is obtained on the basis of low energy singlets and triplets plaquette operators by employing a mean-field approximation. The values of ground state energy and spin gap of this system have been estimated and the validity of this formalism has been tested upon comparison with the known results. Emergence of topological point and line nodes on the basis of spin-disordered ground state noted in this investigation is very rare on any frustrated system as well as the presence of triplet flat band. Evolution of those topological nodes is studied throughout the full frustrated regime. Finally, emergence of topological phases has been reported upon adding a time-reversal-symmetry breaking term to the Hamiltonian. Coexistence of spin gap with either topological nodes or phases turns this honeycomb model an interesting one.

PACS numbers:

I. INTRODUCTION

The observation of magnon Hall effect in ferromagnetic (FM) compound $\text{Lu}_2\text{V}_2\text{O}_7$ has given further impetus toward the investigations of topological phases in magnetic systems¹. Search of topological phases in the antiferromagnetic (AFM) systems begins afterwards as a consequence of this observation. Most of the studies involve in finding nontrivial topology in magnon bands on the basis of spin-ordered ground states. The frustrated AFM systems, on the other hand, very often give rise to exotic spin-disordered ground states those are generally studied in terms of either valence-bond-solid (VBS) or resonating-valence-bond (RVB) states^{2,3}. Thus, search of topological phases nowadays extended beyond the magnetic systems of having spin-ordered ground states. But the finding of topological nontriviality based on the spin-disordered ground state is more challenging for several reasons. In this investigation, emergence of topological point and line nodes along with nontrivial topological phases will be reported in a frustrated AFM spin-1/2 Heisenberg model on the honeycomb lattice where the ground state is a plaquette-VBS (PVBS) state.

In order to investigate the dynamics of the AFM Heisenberg model on the honeycomb lattice a six-spin plaquette operator theory (POT) in terms of triplet plaquette excitations has been developed on the basis of singlet PVBS ground state. Several theoretical approaches have been employed before to study the ground state properties and the dynamics of the AFM J_1 - J_2 model on honeycomb lattice, where, J_1 and J_2 are the nearest (NN) and next-nearest (NNN) neighbor exchange strengths, respectively⁴⁻¹⁶. Most of the studies limit themselves within the moderate frustration range, $0.0 <$

$J_2/J_1 < 0.5$. Existence of three distinct quantum phases has been marked in this regime. One among them is a spin-disordered phase which lies in the intermediate regime, $0.2 < J_2/J_1 < 0.4$, between two different ordered regimes. The ordered phases are gapless Néel and spiral states, which survive in the regions, $0.0 < J_2/J_1 < 0.2$ and $0.4 < J_2/J_1 < 0.5$, respectively. Previous studies have taken this phase diagram for granted with a little dispute on the location of boundaries separating the different phases. The nature of disordered state in the intermediate region is not free of ambiguity as well. But most of the recent studies support the existence of PVBS state^{4,16}. The signature of PVBS phase has been detected in the AFM honeycomb compound $\text{LiZn}_2\text{Mo}_3\text{O}_8$ by measuring the triplet spin gap¹⁷. On the other hand, AFM spin ordered phase has been detected in Na_2IrO_3 , and the thermodynamic properties of this compound have been explained in terms of J_1 - J_2 Heisenberg honeycomb model with $J_2/J_1 = 0.47$ ¹⁸.

In this investigation, POT has been formulated for the entire frustrated regime $0 < J_2/J_1 < 1$ of the model based on two orthogonal plaquette-RVB (PRVB) states, separately for the moderate ($0 < J_2/J_1 < 1/2$) and extreme ($1/2 < J_2/J_1 < 1$) frustrated regimes. Those PRVB states are not only the exact ground states of a single hexagonal plaquette, separately for the two different frustrated regimes but also singlet. Dynamics of the system are studied in terms of a low-energy mean-field Hamiltonian, where dispersion relations of three lowest energy triplets are obtained. Ground state energy and spin gap have been estimated and compared with the numerical results.

Surprisingly, examining the bosonic triplet dispersion relation of this honeycomb model, several types of topo-

logical point and line nodes are found to emerge upon the variation of J_2/J_1 . Two-band and three-band touching points with two different kinds for each one have been noted. Two-band touching nodes are identified as either Dirac or quadratic band touching points (QBTP)¹⁹. Similarly, the three-band touching points in the two regimes are qualitatively different which will be discussed later.

In addition, a flat band and a pair of degenerate Dirac line nodes (DLN) are found in the extreme frustrated regime. DLN is formed when two linear dispersions touch over a line on the Brillouin zone (BZ) rather than at a point. Both the DLNs are topologically protected by the simultaneous existence of space-inversion and time-reversal symmetry (\mathcal{PT} -symmetry) of the system^{20,21}. One Dirac node among all of them is protected by the symmetry of the system, since its position in the BZ is fixed regardless the values of J_2/J_1 , which is analogous to that observed in graphene²². While the remaining nodes are tunable in a sense that their characteristics can be changed by varying the parameters. Thus this frustrated honeycomb model hosts a variety of topological nodes which are not seen before in a single model.

No topological node is found in the bosonic magnon excitation of the AFM Heisenberg model on the honeycomb lattice, though, emergence of a solitary Dirac node is reported in the magnon excitation of a FM Heisenberg model^{23,24}. Additional Weyl nodes emerge when next-next-nearest-neighbor (NNNN) interactions are taken into account in the FM case²³. The magnon DLN is found before in FM Heisenberg model on the three-dimensional (3D) pyrochlore lattice and AFM Heisenberg model on the 2D square-octagon lattice^{21,25}. However, all these topological nodes reported before are based on the spin-ordered ground states. In contrast, all the nodal points and lines emerged in this investigation are based on the spin-disordered ground states.

Chern number (C) acts as an invariant for a particular class of topological phases when the time-reversal symmetry (\mathcal{T} -symmetry) of the system is broken²⁶. Topological protection of the insulating bulk bands is additionally rewarded by the presence of in-gap edge states connecting the separated bands. The value of C and the number of edge state modes are related by the ‘bulk-edge-correspondence’ (BEC) rule²⁷. Previous studies reveal that a gap in the magnon excitation of the FM Heisenberg model opens up at the Dirac nodal point as soon as the NNN Dzyaloshinskii-Moriya interaction (DMI) is invoked, where DMI breaks the space-inversion symmetry (\mathcal{P} -symmetry)²⁴. At the same time, the system becomes topologically nontrivial with $C=\pm 1$. Observation of this particular topological feature has been claimed in the FM honeycomb compound CrI_3 by examining the magnon band obtained in inelastic neutron scattering²⁸. FM Heisenberg models on the honeycomb lattice with Kitaev and spin-anisotropic interactions (SAI) are found to host a number of topological phases^{29,30}. Here, the Zeeman term corresponding to the external magnetic field breaks the \mathcal{T} -symmetry. However, in these cases, topological phases are found in those excitation bands which

are based on the spin-ordered ground states. Also, no topological phase based on AFM spin-ordered ground state is reported on the honeycomb model. Motivated by the emergence of multiple topological nodes of various kinds in this system, the search of Chern insulating phases in the triplet excitation bands based on the disordered ground state has been undertaken in this investigation. The system in the moderate frustrated region is found to host six distinct topological phases when the effective three-band Hamiltonian loses its \mathcal{T} -symmetry invariance.

Two-spin bond operator theory was introduced before by Sachdev and Bhat to study the ground state phase diagram of an AFM Heisenberg model on the square lattice in terms of several VBS states on the basis of various singlet dimer coverings³¹. The method has been extended up to four-spin plaquette operator to study the properties of frustrated AFM Heisenberg models on square-octagon and square lattices based on the PVBS ground states^{32,33}. Upon further extension, POT has been developed on the basis of six-spin frustrated AFM Heisenberg plaquette in this investigation.

The article has been organized in the following way. Properties of a single frustrated Heisenberg hexagonal plaquette is described in the Section II. POT has been described in the Section III. An effective low-energy Hamiltonian in terms of bosonic singlets and triplets operators for J_1 - J_2 AFM Heisenberg model on the honeycomb lattice has been formulated in the Section IV. To estimate the ground state energy and spin gap of the frustrated system a mean-field theory has been developed in the Section V. Emergence and evolution of topological nodal points and lines are described in the Section VI and the properties of topological phases are explained in Section VII. Section VIII holds a comprehensive discussion on the results.

II. SINGLE HEXAGONAL PLAQUETTE

The spin-1/2 AFM Heisenberg Hamiltonian on a single hexagonal plaquette is defined by

$$H^\circ = \sum_{n=1}^6 (J_1 \mathbf{S}^n \cdot \mathbf{S}^{n+1} + J_2 \mathbf{S}^n \cdot \mathbf{S}^{n+2}), \quad \mathbf{S}^{n+6} = \mathbf{S}^n, \quad (1)$$

where \mathbf{S}^n is the spin-1/2 operator at the n -th vertex of the hexagon. So, n runs from 1 to 6, in addition to the periodic boundary condition (PBC). J_1 and J_2 are the respective NN and NNN exchange interaction strengths. J_1 and J_2 compete against each other while computing the minimum value of classical energy of the hexagon, which in other words means that J_2 invokes frustration in this model with respect to J_1 . Here simultaneous minimization of all bond energies fails while constructing the classical ground state, which on the other hand generates highly degenerate ground state. A schematic view of this spin model is shown in Fig 1(a). Thermally stable multipartite entanglement is predicted before in this model

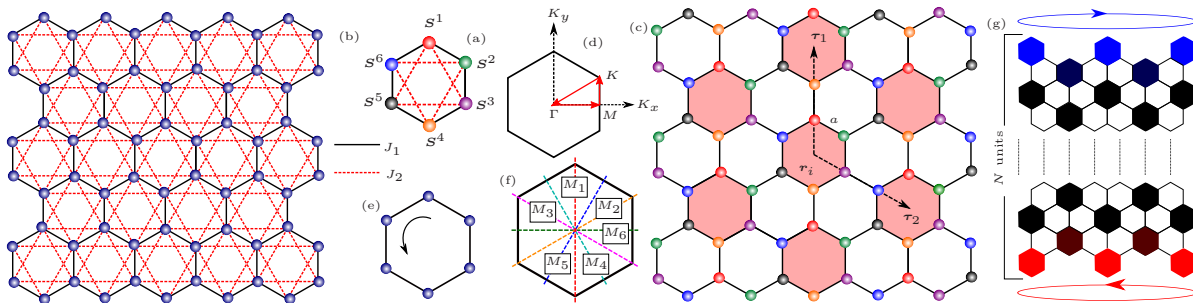


FIG. 1: (a) Geometrical view of the hexagonal plaquette, (b) J_1 - J_2 AFM Heisenberg honeycomb lattice, (c) honeycomb lattice of plaquettes, (d) Brillouin zone of the plaquette honeycomb lattice defined by $\Gamma = (0, 0)$, $M = (\frac{2\pi}{3\sqrt{3}}, 0)$ and $K = (\frac{2\pi}{3\sqrt{3}}, \frac{2\pi}{9})$, (e) system remains invariant under rotation by $\pi/3$, (f) mirror planes are shown by six different dashed lines, (g) strip of honeycomb lattice used for edge state calculation, upper and lower edges are drawn in blue and red colors, respectively.

at the extreme frustrated limit, $J_2/J_1=1$ ³⁴.

The total spin operator, $\mathbf{S}_T = \sum_{n=1}^6 \mathbf{S}^n$, as well as z -component of the total spin, S_T^z , commute with the Hamiltonian, H° , since the system is $SU(2)$ invariant. The eigenvalue equation of H° has been solved exactly by spanning the Hamiltonian matrix separately into the subspaces for different S_T^z values as they are being good quantum numbers. The Hilbert space of this six-spin Hamiltonian consists of 2^6 states and those states comprise to five singlets ($S_T = 0$), nine triplets ($S_T = 1$), five quintets ($S_T = 2$) and one septet ($S_T = 3$). The exact analytic expressions of all singlet ($|s\rangle$), triplet ($|t\rangle$), quintet ($|q\rangle$) and septet ($|h\rangle$) states with energy eigenvalues have been listed in the Appendix A. Six pairs of doubly-degenerate states are there. One singlet pair, three triplet pairs and two quintet pairs are found to be degenerate. Among those singlets, only two, $|s_{1-}\rangle$ and $|s_{2-}\rangle$ can be expressed in terms of Kekule configurations. So, they can be recognized as RVB states for a single hexagon. Those two particular singlets are denoted by Ψ_{RVB} and Ψ'_{RVB} , respectively. The pictorial views of those states, Ψ_{RVB} ($|s_{1-}\rangle$) and Ψ'_{RVB} ($|s_{2-}\rangle$) are shown in Fig 2. Ψ_{RVB} is symmetric, whereas, Ψ'_{RVB} is antisymmetric under the reflection about the mirror planes passing through any vertices of the hexagon. Those mirror planes are shown by dashed lines noted with M_1 , M_2 and M_3 in Fig 1 (f). While both the RVB states are antisymmetric under spin inversion as well as reflection about the mirror planes normal to any NN bonds of the hexagon (\mathcal{M} -symmetry). Those mirror planes are shown by dashed lines marked with M_4 , M_5 and M_6 in Fig 1 (f). Rotation and reflection symmetries of all the eigenstates are described in the Appendix A.

Variation of all those energy eigenvalues against J_2/J_1 is shown in Fig 3 (a). Several crossovers among the energy states are found with the change of J_2/J_1 . Energy states below the dashed line are considered to develop the POT. An expanded view of the region below the dashed line is separately shown in Fig 3 (b). The variation of energies for two lowest singlets, $|s_{1-}\rangle$ and $|s_{2-}\rangle$, along with that of three lowest triplets, $|t_{1-,\alpha}\rangle$ and doubly

$$\Psi_{\text{RVB}} \equiv -\sqrt{\frac{2}{3}} \frac{1}{\mu_{s_{1-}}} \left[\text{Kekule}_1 + \text{Kekule}_2 - \sqrt{2} C_{s_{1-},3} \text{Central}_1 \right],$$

$$\Psi'_{\text{RVB}} \equiv \sqrt{\frac{2}{3}} \left[\text{Kekule}_3 - \text{Kekule}_4 \right] + \frac{1}{\sqrt{2}} \begin{pmatrix} \uparrow\downarrow & \downarrow\uparrow \\ i & j \\ j & i \end{pmatrix},$$

$$C_{s_{1-},3} = \frac{-\sqrt{2}(2J_2 - J_1)}{(3J_1 - J_2 + d_s)}, \quad d_s = \sqrt{13J_1^2 + 9J_2^2 - 18J_1J_2},$$

$$C_{s_{1-},1} = \frac{-\sqrt{6}J_1}{(-J_1 + 3J_2 + d_s)}, \quad \mu_{s_{1-}} = \sqrt{1 + C_{s_{1-},1}^2 + C_{s_{1-},3}^2}.$$

FIG. 2: Pictorial representation of Ψ_{RVB} and Ψ'_{RVB} . Arrow indicates the spin ordering in a singlet dimer bond.

degenerate $|t_{2-,\alpha}\rangle$, $|t_{3-,\alpha}\rangle$, are plotted in Fig 3 (b). Here, $\alpha = x, y, z$, denotes the three different components of the triplet state. In this region of energy, one singlet-singlet ($|s_{1-}\rangle$ - $|s_{2-}\rangle$) and one singlet-triplet ($|s_{2-}\rangle$ - $|t_{1-,\alpha}\rangle$) crossovers are observed.

$E_{s_{1-}}$ and $E_{s_{2-}}$ are the energies of the singlet states $|s_{1-}\rangle$ and $|s_{2-}\rangle$, respectively. Similarly, $E_{t_{1-}}$ and $E_{t_{2-}} = E_{t_{3-}}$ are the energies of the triplet states $|t_{1-,\alpha}\rangle$ and doubly degenerate $|t_{2-,\alpha}\rangle$, $|t_{3-,\alpha}\rangle$, respectively. Ground state is always a total spin singlet. Two RVB states form the ground states in two different regions, say, R_1 and R_2 . In the moderate frustrated region (R_1), $0 < J_2/J_1 < 1/2$ where Ψ_{RVB} or $|s_{1-}\rangle$ is the ground state, while Ψ'_{RVB} or $|s_{2-}\rangle$ is that in the extreme frustrated region (R_2) when $1/2 < J_2/J_1 < 1$. Energies of these two singlets cross themselves at the point $J_2/J_1 = 1/2$. So, ground state is doubly degenerate at this point. This figure reveals that two types of spin gaps are there for a single hexagonal plaquette, those are associated with the transitions between two different sets of lowest energy states. One is associated with a singlet-triplet transition (triplet gap) when $J_2/J_1 < 1/4$ while other one is a singlet-singlet (singlet gap) when $J_2/J_1 > 1/4$. Three triplet and one singlet states are found degenerate at the point $J_2/J_1 = 1$. Based on these lowest energy singlet and triplet states,

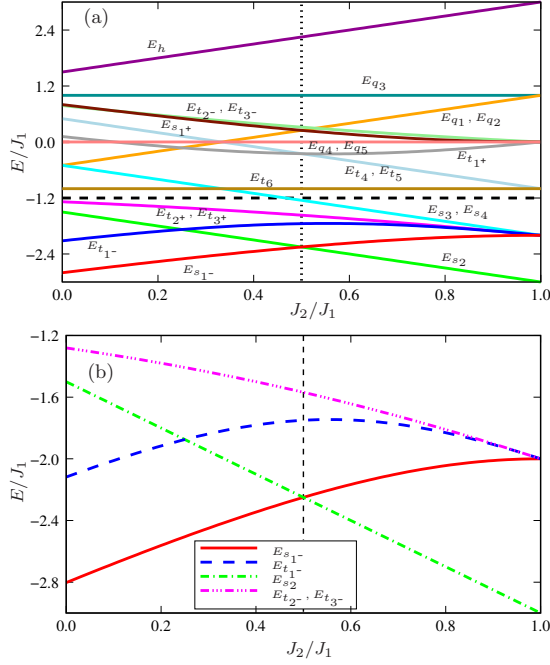


FIG. 3: Variation of energy eigenvalues of single plaquette against J_2/J_1 .

POT has been developed to study the properties of PVBS phase of this frustrated honeycomb model. In this theoretical development, singlets Ψ_{RVB} and Ψ'_{RVB} get condensed separately in the regions R_1 and R_2 , respectively. Thus in the PVBS phase, ground state is actually the product of respective PRVB states defined on a regular array of plaquettes. One such array is shown in Fig 1 (c). As a result, ground state is six-fold degenerate and preserve the symmetry of the Hamiltonian in every case^{2,3}.

III. PLAQUETTE OPERATOR THEORY

In order to develop the POT, all the six spin-1/2 operators within each individual hexagonal plaquette, *i.e.*, S^n , $n = 1, 2, \dots, 6$, are expressed in terms of the creation operators of a number of low energy eigenstates of H° . Those states are chosen from the complete list available in the Appendix A. As the true Hilbert space of a single plaquette consists of 64 states, the corresponding 64 creation operators are defined by the following notations.

$$\begin{aligned} |s_j\rangle &= s_j^\dagger |0\rangle, |t_{a,\alpha}\rangle = t_{a,\alpha}^\dagger |0\rangle, |q_{b,\nu}\rangle = q_{b,\nu}^\dagger |0\rangle, \\ |q_{b,\alpha}\rangle &= q_{b,\alpha}^\dagger |0\rangle, |h_\zeta\rangle = h_\zeta^\dagger |0\rangle, |h_\alpha\rangle = h_\alpha^\dagger |0\rangle, \end{aligned} \quad (2)$$

where $|0\rangle$ denotes the vacuum state. All the operators are assumed to satisfy the bosonic commutation relations whenever defined for the same plaquette, otherwise commute when they are specified for the different plaquettes.

The alphabets, s, t, q and h stand for the singlet, triplet, quintet and septet states, respectively. Subscripts, $j = 1^\pm, 2, 3, 4$, $a = 1^\pm, 2^\pm, 3^\pm, 4, 5, 6$, and $b = 1, 2, 3, 4, 5$, indicate five singlets, nine triplets and five quintets, respectively. Additional subscripts $\alpha = x, y, z$, $\nu = 1^\pm$, and $\zeta = 1^\pm, 2^\pm$, denote the components of those multiplets. The peculiar combinations of numbers and signs for j and a are found useful to write down the corresponding eigenstates and eigenvalues in a compact form. The similar argument does hold in a different way for the additional subscripts, $\alpha = x, y, z$, $\nu = 1^\pm$, and $\zeta = 1^\pm, 2^\pm$. Precisely, the particular index \pm is used for bunching up a pair of eigenstates in a single expression and so the individual sign does not correspond to eigenvalue of parity or any other operators. Anyway, the completeness relation in this full Hilbert space is thus given by

$$\begin{aligned} \sum_j s_j^\dagger s_j + \sum_{a,\alpha} t_{a,\alpha}^\dagger t_{a,\alpha} + \sum_{b,\nu} q_{b,\nu}^\dagger q_{b,\nu} + \sum_{b,\alpha} q_{b,\alpha}^\dagger q_{b,\alpha} \\ + \sum_\zeta h_\zeta^\dagger h_\zeta + \sum_\alpha h_\alpha^\dagger h_\alpha = 1. \end{aligned} \quad (3)$$

The Hamiltonian (Eq 1) in the full Hilbert space assumes the form

$$\begin{aligned} H^\circ = \sum_j E_{s_j} s_j^\dagger s_j + \sum_{a,\alpha} E_{t_a} t_{a,\alpha}^\dagger t_{a,\alpha} + \sum_{b,\nu} E_{q_b} q_{b,\nu}^\dagger q_{b,\nu} \\ + \sum_{b,\alpha} E_{q_b} q_{b,\alpha}^\dagger q_{b,\alpha} + E_h \sum_\zeta h_\zeta^\dagger h_\zeta + E_h \sum_\alpha h_\alpha^\dagger h_\alpha. \end{aligned} \quad (4)$$

However, the spin operators, S_α^n , are expressed in the Fock space constituted by a limited number of plaquette operators as shown below

$$\begin{aligned} S_\alpha^n = A_\eta^n \left(t_{\eta^-,\alpha}^\dagger s_{1^-} + s_{1^-,\eta}^\dagger t_{\eta^-,\alpha} \right) + B_\eta^n \left(t_{\eta^-,\alpha}^\dagger s_2 + s_2^\dagger t_{\eta^-,\alpha} \right) \\ - i \epsilon_{\alpha\beta\gamma} D_{\eta\xi}^n t_{\eta^-,\beta}^\dagger t_{\xi^-, \gamma}. \end{aligned} \quad (5)$$

Here, n , again denotes the position of spin within a plaquette, $\alpha = x, y, z$, $\eta = 1, 2, 3$, and $\xi = 1, 2, 3$. The matrix elements, $A_\eta^n = \langle s_{1^-} | S_\alpha^n | t_{\eta^-,\alpha} \rangle$, $B_\eta^n = \langle s_2 | S_\alpha^n | t_{\eta^-,\alpha} \rangle$, and $D_{\eta\xi}^n = \langle t_{\xi^-, \gamma} | S_\alpha^n | t_{\eta^-, \beta} \rangle$, are given in the Appendix B. The reduced space is spanned by the two lowest singlets, $(|s_{1^-}\rangle, |s_2\rangle)$, and three lowest triplets, $(|t_{1^-,\alpha}\rangle, |t_{2^-,\alpha}\rangle, |t_{3^-,\alpha}\rangle)$, those are shown in Fig 3 (b). Therefore, the spin commutation relations, $[S_\alpha^n, S_\beta^m] = i \epsilon_{\alpha\beta\gamma} \delta_{nm} S_\gamma^n$, will be preserved by taking into account the completeness relation in the truncated Hilbert space, which reads as,

$$\sum_{j=1^-,2} s_j^\dagger s_j + \sum_{\eta,\alpha} t_{\eta^-,\alpha}^\dagger t_{\eta^-,\alpha} = 1. \quad (6)$$

The form of S_α^n that is given in Eq 5 has been used to express the inter-plaquette interactions in the AFM Heisenberg Hamiltonian for the honeycomb lattice. Thus, the low-energy dynamics of bosonic version of this model will be studied in this truncated Hilbert space. Nevertheless, a more general form of the spin operators, S_α^n in terms of all singlets and triplets are available in the Appendix B.

IV. THE LOW ENERGY BOSON MODEL

In this section, POT has been employed to study the PVBS phase of the J_1 - J_2 AFM Heisenberg honeycomb model. The non-Bravais honeycomb lattice is assumed as a triangular lattice composed of hexagonal plaquettes as shown in Fig 1(b). The Hamiltonian is expressed in terms of spin operators those are assigned to a definite site of a particular plaquette which is constituted by six different sites.

$$\begin{aligned}
H = \sum_i & [H_{r_i}^O + J_1 (\mathbf{S}_{r_i}^1 \cdot \mathbf{S}_{r_i+\tau_1}^4 + \mathbf{S}_{r_i}^2 \cdot \mathbf{S}_{r_i+\tau_1+\tau_2}^5 + \mathbf{S}_{r_i}^3 \cdot \mathbf{S}_{r_i+\tau_2}^6) \\
& + J_2 (\mathbf{S}_{r_i}^1 \cdot \mathbf{S}_{r_i+\tau_1}^5 + \mathbf{S}_{r_i}^1 \cdot \mathbf{S}_{r_i+\tau_1}^3 + \mathbf{S}_{r_i}^1 \cdot \mathbf{S}_{r_i+\tau_1+\tau_2}^5 \\
& + \mathbf{S}_{r_i}^2 \cdot \mathbf{S}_{r_i+\tau_1}^4 + \mathbf{S}_{r_i}^2 \cdot \mathbf{S}_{r_i+\tau_1+\tau_2}^6 + \mathbf{S}_{r_i}^2 \cdot \mathbf{S}_{r_i+\tau_1+\tau_2}^4 \\
& + \mathbf{S}_{r_i}^2 \cdot \mathbf{S}_{r_i+\tau_2}^6 + \mathbf{S}_{r_i}^3 \cdot \mathbf{S}_{r_i+\tau_1+\tau_2}^5 + \mathbf{S}_{r_i}^3 \cdot \mathbf{S}_{r_i+\tau_2}^1 \\
& + \mathbf{S}_{r_i}^3 \cdot \mathbf{S}_{r_i+\tau_2}^5 + \mathbf{S}_{r_i}^4 \cdot \mathbf{S}_{r_i+\tau_2}^6 + \mathbf{S}_{r_i}^6 \cdot \mathbf{S}_{r_i+\tau_1}^4)]. \quad (7)
\end{aligned}$$

Here, the vector \mathbf{r}_i indicates the position of a particular plaquette while the other two vectors, $\boldsymbol{\tau}_1$ and $\boldsymbol{\tau}_2$ are used to point the positions of surrounding plaquettes in the resulting triangular lattice. $\mathbf{S}_{\mathbf{r}}^n$ denotes the spin-1/2 operator at the n -th vertex of the hexagonal plaquette at the position \mathbf{r} . Therefore, in this case, $\boldsymbol{\tau}_1$ and $\boldsymbol{\tau}_2$ could be considered as the primitive vectors in this effective triangular lattice formed by the hexagonal plaquettes. They can be expressed in the following way:

$$\boldsymbol{\tau}_1 = 3a \hat{y} \quad \text{and} \quad \boldsymbol{\tau}_2 = \frac{3\sqrt{3}a}{2} \hat{x} - \frac{3a}{2} \hat{y}, \quad (8)$$

where a is the NN lattice spacing of the original honeycomb lattice which is henceforth assumed to be unity. The Hamiltonian H is SU(2) invariant. Ultimately, H is expressed in terms of singlet and triplet plaquette operators when the $\mathbf{S}_{\mathbf{r}}^n$ is replaced by bosonic plaquette operators using the Eq 5, and thus has the following form:

$$H = E_0 + H_{02} + H_{20} + H_{30} + H_{21} + H_{40} + H_{22}. \quad (9)$$

Obviously, H_{nm} indicates different terms in the Hamiltonian in which E_0 is a constant. The expression of relevant terms in the momentum space will be shown in the next section. In H_{nm} , n and m indicate the numbers of triplet and singlet operators, respectively. Expressions of H_{nm} with non-zero value of m will be different for the regions R_1 and R_2 those are introduced before in the Sec II. Value of E_0 will be different in the regions R_1 and R_2 . It should be noted that the Hamiltonian is expressed in terms of the two lowest energy singlets and three lowest energy triplets only. The contribution of higher energy singlets and triplets as well as all quintets and the septet is neglected. So, the truncated form of the relevant constraint (Eq 6) has been taken into account by adding the following term to the Hamiltonian (Eq 9),

$$-\mu \sum_i \left(\sum_{j=1^-,2} s_{j,i}^\dagger s_{j,i} + \sum_{\eta,\alpha} t_{\eta^-,i,\alpha}^\dagger t_{\eta^-,i,\alpha} - 1 \right), \quad (10)$$

where μ is the Lagrange multiplier. The summation index i runs over the all triangular lattice sites. Here μ can be imagined as the chemical potential which is assumed to be site independent in accordance with the translational invariance of the system.

To study the low-energy dynamics of this system, the effective Hamiltonian is derived by condensing the lowest energy RVB states, $|s_{1^-,i}\rangle$ and $|s_{2,i}\rangle$ in every site i for the respective parameter regimes R_1 and R_2 , separately. Thus, for the implementation of plaquette operator formalism, one of the two singlet states $|s_{j,i}\rangle$, $j = 1^-, 2$, is assumed to be condensed and so has been substituted by a number, \bar{s} in Eq 9. The effect of condensation is thus taken into account by making the following replacement, $s_{j,i}^\dagger = s_{j,i} = \langle s_{j,i}^\dagger \rangle = \langle s_{j,i} \rangle = \bar{s}^{31}$.

As a result, the effective Hamiltonian contains the operators related to the singlet $|s_{2,i}\rangle$, ($|s_{1^-,i}\rangle$) in R_1 , (R_2) along with the three triplets. Now the value of the constant, E_0 is given by the equation, $E_0 = N' [\bar{s}^2 E - \mu (\bar{s}^2 - 1)]$, in which $E = E_{s_{1^-}} - (E_{s_2})$ for the region R_1 (R_2). $N' = N/6$ where N is the total number of sites of the original honeycomb lattice. Fourier transformation of the operators $t_{\eta^-,i,\alpha}^\dagger$ and $s_{j,i}^\dagger$ are

$$\begin{aligned}
t_{\eta^-,i,\alpha}^\dagger &= \frac{1}{\sqrt{N'}} \sum_{\mathbf{k}} \exp(-i\mathbf{k} \cdot \mathbf{R}_i) t_{\eta^-,\mathbf{k},\alpha}^\dagger, \\
s_{j,i}^\dagger &= \frac{1}{\sqrt{N'}} \sum_{\mathbf{k}} \exp(-i\mathbf{k} \cdot \mathbf{R}_i) s_{j,\mathbf{k}}^\dagger.
\end{aligned} \quad (11)$$

Here, the momentum sum runs over the BZ of the triangular lattice.

V. MEAN-FIELD ANALYSIS

In order to estimate the ground state energy, E_G and the singlet to triplet spin gap, Δ , of the honeycomb model, a mean-field theory has been developed. Triplet dispersion relations based on the PVBS ground state are obtained. Hamiltonian retains upto the quadratic terms, as a result, the terms $H_{30}, H_{21}, H_{40}, H_{22}$ have been neglected. However, expressions of those terms in the momentum space are available in the Appendix C. Now the mean-field Hamiltonian becomes,

$$H_{MF} = E_0 + H_{02} + H_{20}. \quad (12)$$

This truncated Hamiltonian is capable to capture the low energy dynamics of the system valid at the low temperatures. The expressions of H_{02} and H_{20} in terms of singlet and triplet operators in momentum space become

$$H_{02} = \sum_{\mathbf{k}} (E_{s_m} - \mu) s_{m,\mathbf{k}}^\dagger s_{m,\mathbf{k}}, \quad (13)$$

with $m = 2$ and 1^- for the regions R_1 and R_2 , respectively.

$$H_{20} = \sum_{\mathbf{k}, \eta, \xi} X_{\mathbf{k}}^{\eta\xi} t_{\eta^-, \mathbf{k}, \alpha}^\dagger t_{\xi^-, \mathbf{k}, \alpha} + \frac{Y_{\mathbf{k}}^{\eta\xi}}{2} \left(t_{\eta^-, \mathbf{k}, \alpha}^\dagger t_{\xi^-, -\mathbf{k}, \alpha} + t_{\eta^-, -\mathbf{k}, \alpha} t_{\xi^-, \mathbf{k}, \alpha} \right), \quad (14)$$

where, $\eta, \xi = 1, 2, 3$ and $\alpha = x, y, z$. The coefficients $X_{\mathbf{k}}^{\eta\xi}$ and $Y_{\mathbf{k}}^{\eta\xi}$ are given in Appendix C. H_{02} is already diagonalized in the singlet basis space where the singlet excitation energy is $\Omega_s = (E_{s_m} - \mu)$. The six-component vector $\Psi_{\mathbf{k},\alpha}^\dagger = \left(t_{1^-, \mathbf{k}, \alpha}^\dagger, t_{2^-, \mathbf{k}, \alpha}^\dagger, t_{3^-, \mathbf{k}, \alpha}^\dagger, t_{1^-, -\mathbf{k}, \alpha}, t_{2^-, -\mathbf{k}, \alpha}, t_{3^-, -\mathbf{k}, \alpha} \right)$ is introduced to diagonalize H_{20} in the basis space comprised of three different triplets. Thus, the matrix form of Eq 12 looks like

$$H_{\text{MF}} = E'_0 + H_{02} + \frac{1}{2} \sum_{\mathbf{k}} \Psi_{\mathbf{k},\alpha}^\dagger H_{\mathbf{k}} \Psi_{\mathbf{k},\alpha}, \quad (15)$$

where

$$E'_0 = E_0 - \frac{3}{2} \sum_{\mathbf{k}} \sum_{\eta=1,2,3} X_{\mathbf{k}}^{\eta\eta}, \quad (16)$$

and $H_{\mathbf{k}}$ is a 6×6 matrix. $H_{\mathbf{k}}$ has the following form when expressed in terms of two symmetric submatrices, $X_{\mathbf{k}}$ and $Y_{\mathbf{k}}$.

$$H_{\mathbf{k}} = \begin{pmatrix} X_{\mathbf{k}} & Y_{\mathbf{k}} \\ Y_{\mathbf{k}} & X_{\mathbf{k}} \end{pmatrix}. \quad (17)$$

The elements of $X_{\mathbf{k}}$ and $Y_{\mathbf{k}}$ are $X_{\mathbf{k}}^{\eta\xi}$ and $Y_{\mathbf{k}}^{\eta\xi}$, respectively, where all of them are real. In addition, all the respective off-diagonal elements of $X_{\mathbf{k}}$ and $Y_{\mathbf{k}}$ are the same. After diagonalization, the Hamiltonian assumes the form³⁵

$$H_{\text{MF}} = E_G + H_{02} + \frac{1}{2} \sum_{\mathbf{k}} \Phi_{\mathbf{k},\alpha}^\dagger H'_{\mathbf{k}} \Phi_{\mathbf{k},\alpha}, \quad (18)$$

where the expression of ground state energy is

$$E_G = E_0 + \frac{3}{2} \sum_{\eta,\mathbf{k}} (\Omega_{\eta,\mathbf{k}} - X_{\mathbf{k}}^{\eta\eta}). \quad (19)$$

The diagonalized matrix in this case looks like

$$H'_{\mathbf{k}} = \begin{pmatrix} h_{\mathbf{k}} & 0 \\ 0 & -h_{\mathbf{k}} \end{pmatrix} \text{ where } h_{\mathbf{k}} = \begin{pmatrix} \Omega_{1,\mathbf{k}} & 0 & 0 \\ 0 & \Omega_{2,\mathbf{k}} & 0 \\ 0 & 0 & \Omega_{3,\mathbf{k}} \end{pmatrix}.$$

Again, each triplet dispersion, $\Omega_{\eta,\mathbf{k}}$, $\eta = 1, 2, 3$, is triply degenerate, since the Hamiltonian (Eq 7) is SU(2) invariant. The eigenvectors $\Phi_{\mathbf{k},\alpha}^\dagger$ is given by $\Phi_{\mathbf{k},\alpha}^\dagger = \left(b_{1^-, \mathbf{k}, \alpha}^\dagger, b_{2^-, \mathbf{k}, \alpha}^\dagger, b_{3^-, \mathbf{k}, \alpha}^\dagger, b_{1^-, -\mathbf{k}, \alpha}, b_{2^-, -\mathbf{k}, \alpha}, b_{3^-, -\mathbf{k}, \alpha} \right)$. Two sets of boson operators t_{η^-} and b_{η^-} , ($\eta = 1, 2, 3$), are connected to each other by the following relation³⁵,

$$\Phi_{\mathbf{k},\alpha} = M_{\mathbf{k}} \Psi_{\mathbf{k},\alpha}, \quad \text{where } M_{\mathbf{k}} = \begin{pmatrix} U_{\mathbf{k}}^\dagger & -V_{\mathbf{k}}^\dagger \\ -V_{\mathbf{k}}^\dagger & U_{\mathbf{k}}^\dagger \end{pmatrix}. \quad (20)$$

Coefficients of the 3×3 Hermitian matrices $U_{\mathbf{k}}^\dagger$ and $V_{\mathbf{k}}^\dagger$ are the Bogoliubov coefficients $u_{\mathbf{k}}^{\eta\xi}$ and $v_{\mathbf{k}}^{\eta\xi}$, respectively. The analytic expressions of the triplet excitation energies $\Omega_{\eta,\mathbf{k}}$ and the Bogoliubov coefficients $u_{\mathbf{k}}^{\eta\xi}$ and $v_{\mathbf{k}}^{\eta\xi}$ written in terms of the components $X_{\mathbf{k}}^{\eta\xi}$ and $Y_{\mathbf{k}}^{\eta\xi}$ are available in Appendix C.

Two self-consistent equations for the determination of mean-field parameters, μ and \bar{s}^2 are obtained by minimizing the ground state energy, E_G , with respect to themselves as $\frac{\partial E_G}{\partial \mu} = 0$, and $\frac{\partial E_G}{\partial \bar{s}^2} = 0$. The resulting equations are

$$\begin{aligned} \mu &= E + \frac{3}{2N'} \sum_{\eta,\mathbf{k}} \left[\frac{\partial \Omega_{\eta,\mathbf{k}}}{\partial \bar{s}^2} - \frac{Y_{\mathbf{k}}^{\eta\eta}}{\bar{s}^2} \right], \\ \bar{s}^2 &= 1 + \frac{3}{2N'} \sum_{\eta,\mathbf{k}} \left[\frac{\partial \Omega_{\eta,\mathbf{k}}}{\partial \mu} + 1 \right]. \end{aligned} \quad (21)$$

Again, $m = 2$ and 1^- for the regions R_1 and R_2 , respectively. By substituting the numerical values of μ and \bar{s}^2 the singlet, $\Omega_{s_m} = E_{s_m} - \mu$, and the three triplet, $\Omega_{\eta,\mathbf{k}}$, $\eta = 1, 2, 3$, excitation energies have been obtained. Value of \bar{s}^2 is always positive as expected and less than unity, while μ is always negative. The singlet excitations, Ω_{s_m} are found to be always dispersionless in the mean-field approximation. The self-consistent equations do not converge in the region $0.0 \leq J_2/J_1 \leq 0.11$. This type of non-convergence in the mean-field procedure for the plaquette and bond-operator theories have been reported before^{33,36}. Triplet dispersion along with the evolution of topological nodes are discussed in the next section (Sec VI).

The value of Δ has been obtained by measuring the energy difference between the ground and the lowest triplet states. Energy of the triplet dispersion, $\Omega_{3,\mathbf{k}}$, is always lower than those of other triplets, $\Omega_{1,\mathbf{k}}$ and $\Omega_{2,\mathbf{k}}$. Variation of $\Omega_{3,\mathbf{k}}$ in the BZ indicates that minima of $\Omega_{3,\mathbf{k}}$ happens to occur at the symmetric points Γ , M and K in the BZ. Thus variation of excitation energies for $\Omega_{3,\Gamma}$, $\Omega_{3,M}$ and $\Omega_{3,K}$ with respect to J_2/J_1 have been plotted in in Figs 4 (a) and 4 (b) for the regions R_1 and R_2 , respectively, along with that of Ω_{s_m} . Those energies are measured with respect to the ground state energy. By comparing the energies of $\Omega_{3,\Gamma}$, $\Omega_{3,M}$ and

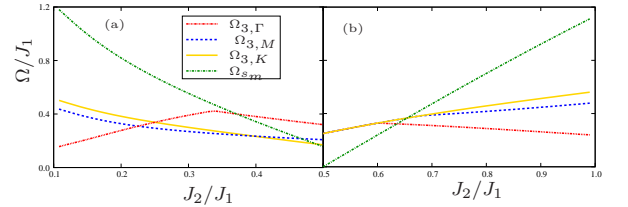


FIG. 4: Variation of excitation energies for $\Omega_{3,\Gamma}$, $\Omega_{3,M}$ and $\Omega_{3,K}$ with respect to E_G against J_2/J_1 (a) in region R_1 , (b) in region R_2 .

$\Omega_{3,K}$ in the region R_1 , it is evident that $\Omega_{3,\Gamma}$, $\Omega_{3,M}$ and $\Omega_{3,K}$ are the lowest when $0.11 < J_2/J_1 < 0.23$, $0.23 < J_2/J_1 < 0.40$ and $0.40 < J_2/J_1 < 0.50$, respectively. In region R_2 , $\Omega_{3,\Gamma}$, $\Omega_{3,M}$ and $\Omega_{3,K}$ have the same value for $0.5 < J_2/J_1 < 0.66$, and thereafter $\Omega_{3,\Gamma}$ is the lowest. The value of Δ has been estimated from this comparative study.

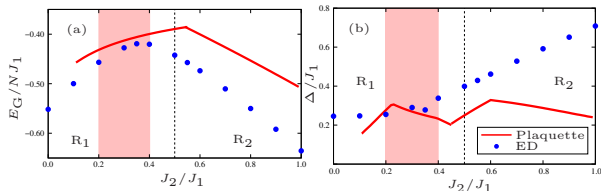


FIG. 5: Variation of (a) Ground-state energy per site and (b) spin gap against J_2/J_1 . The shaded region indicates the PVBS phase.

Variation of ground state energy per site with respect to J_2/J_1 is shown in Fig 5(a). Result based on the POT is plotted in red line and that has been compared with the exact diagonalization data for $N=32$ sites shown in blue points³⁷. The value of E_G/NJ_1 shows closer agreement with the exact diagonalization data in the disordered PVBS phases which is identified by the region shaded in pink, where this formalism stands valid. However, the ground state energy is always higher than the true value because of the fact that POT is basically a variational approach. E_G/NJ_1 shows significant departure from the exact diagonalization data in the ordered regions since POT fails to capture the quantum correlation in those regions. Similarly, spin gap (Δ/J_1) has been evaluated through the POT and that is shown in Fig 5(b). The estimated value of spin gap in the PVBS phase (shaded in pink) is significantly close to the numerical values. In addition to that, gap is also found in the magnetic ordered phases which are supposed to be gapless. Δ/J_1 corresponds to the gap between the ground state energy and the minimum of the triplet excitations. More accurate estimation of the ground state energy and the spin gap can be made in this formalism by accommodating the higher energy modes of the single plaquette excitations in the POT those are neglected before.

VI. TRIPLET DISPERSIONS AND TOPOLOGICAL MODES

Two different kinds of band-touching points or nodes, are noted depending on the number of meeting bands. They are termed as two-band and three-band touching points (TBTP), where two and three bands are found to meet there, respectively. Two types of two-band touching points are identified depending on their nature of dispersion relation around the respective touching points. Those nodes are called Dirac and QBTP. For the QBTP, energy of triplet excitation is proportional to square of the momentum in the vicinity of the touching point. The QBTP can be regarded as a pair of Dirac nodes¹⁹. Similarly, two types of TBTP are identified for the same reason as stated before. It has been noted that energy of triplet excitation of all the three meeting bands are proportional to the square of the momentum in the neighborhood of the touching point for the case of TBTP in the

region R_1 . On the other hand, the lowest energy band is flat for the TBTP found in the region R_2 . Energy of triplet dispersion of the remaining two meeting bands are proportional to the square of the momentum near the touching point in this case. Emergence and evolution of those point nodes as well as the DLNs with the variation of J_2/J_1 have been shown in Fig 6. Dirac, QBTP and TBTP appear both in the regions R_1 and R_2 , while DLN and flat band appear only in the region R_2 .

The 3D plot of the triplet dispersions for the region R_1 have been shown in Fig 7(a)-(c). Those figures are supplemented by the respective dispersion along the high-symmetry pathway (Γ, M, K, Γ), density of states (DOS), as well as the location of topological nodes within the BZ. DOS is useful to estimate the values of band gap and band width. The number of band touching points changes with J_2/J_1 , however, a Dirac node is always formed due to the band touching of upper two bands at the K point regardless the values of J_2/J_1 , which is denoted by black circle in the figures. So, this particular node is protected by the symmetry of the Hamiltonian, while other nodes appear as a result of accidental degeneracy.

Closer view of this Dirac node is shown in Fig 8. This particular Dirac node is analogous to that appeared in graphene²². Thus it can be regarded as a generic feature of the honeycomb lattice. The same Dirac node is found in the triplet magnon excitation of the FM Heisenberg model in the collinear phase, though it is absent in the AFM case²³. This discrepancy is attributed to the fact that FM ground state does not break the \mathcal{M} -symmetry, while the AFM ground state does²³. It is worth mentioning in this situation that FM state is the exact ground state of the Hamiltonian, while the AFM state is not the exact one. On the other hand, under the same mirror reflection, both Ψ_{RVB} and Ψ'_{RVB} states are antisymmetric. Further, the PVBS ground states preserve the symmetry of the Hamiltonian. As a result, this particular Dirac node in the triplet dispersion is present in both the regions R_1 and R_2 , irrespective of the values of exchange strengths.

The TBTP is noticed at the Γ point only when $J_2/J_1 = 0.337$, whereas a QBTP between upper two band is found at that point when $J_2/J_1 < 0.337$, by leaving a gap between the lower two bands. This QBTP always appears at the Γ point irrespective of the values of J_2/J_1 , as long as $J_2/J_1 < 0.337$. On the other hand, six pairs of Dirac nodes are found to appear with equal share between the lower and upper two bands, as soon as $J_2/J_1 > 0.337$, along with the emergence of another QBTP between the lower two bands at the Γ point. These additional Dirac nodes are found to emerge in the immediate vicinity of the Γ point, while the QBTP originates at the Γ point itself. Although the Dirac nodes shift towards the M (upper Dirac nodes) and K (lower Dirac nodes) points with the increase of J_2/J_1 , the QBTP does not change its position. This picture is valid for the region, $0.337 < J_2/J_1 < 0.50$. Locations of those movable nodes in the BZ and dispersion along (Γ, M, K, Γ) path-

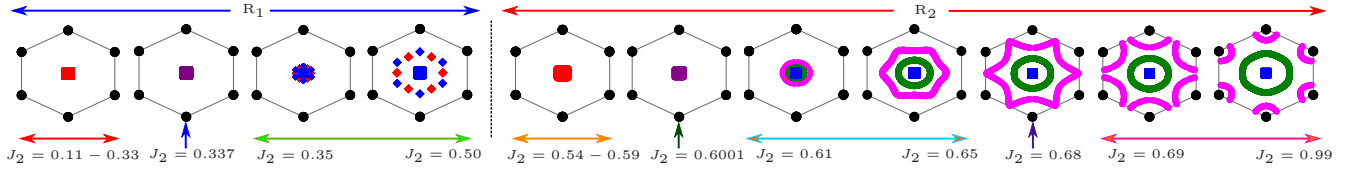


FIG. 6: Kaleidoscope of the imprints of evolutionary nodes and nodal lines on the BZ with the change of J_2/J_1 , where $J_1 = 1$.

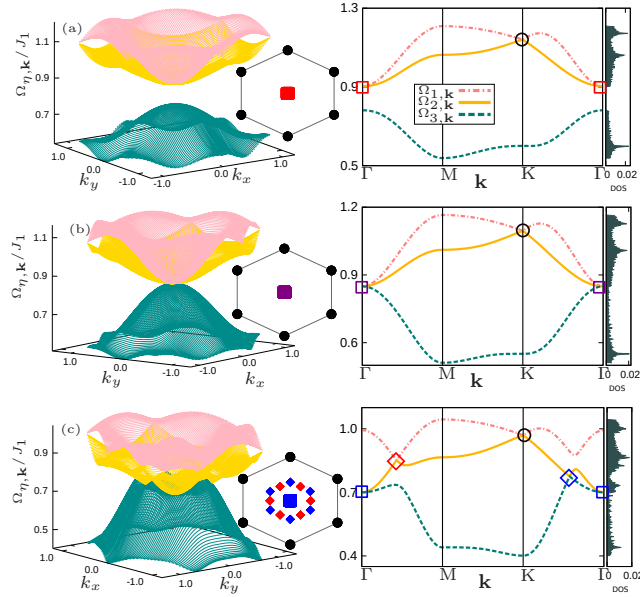


FIG. 7: Evolution of nodes in region R_1 with J_2/J_1 , $J_2/J_1 =$ (a) 0.30, (b) 0.337, (c) 0.45.

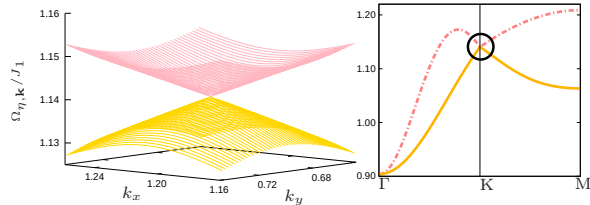


FIG. 8: Closer view of triplet excitations around the Dirac node when $J_2/J_1 = 0.30$.

way are marked by red and blue diamonds, for the Dirac nodes in between upper and lower two bands, respectively. Therefore, the TBTP (purple square) at the Γ point for $J_2/J_1 = 0.337$ is replaced by QBTP between upper bands (red square) and that between lower bands (blue square) for $J_2/J_1 < 0.337$ and $J_2/J_1 > 0.337$, respectively. Closer view of triplet excitations around those QBTPs are shown in Fig 9 (a) and (b), at two definite values, $J_2/J_1 = 0.30$ and $J_2/J_1 = 0.45$, respectively. No band gap is found in the regime, $0.337 \leq J_2/J_1 < 0.50$.

As a result, the fixed Dirac node at the K point (black

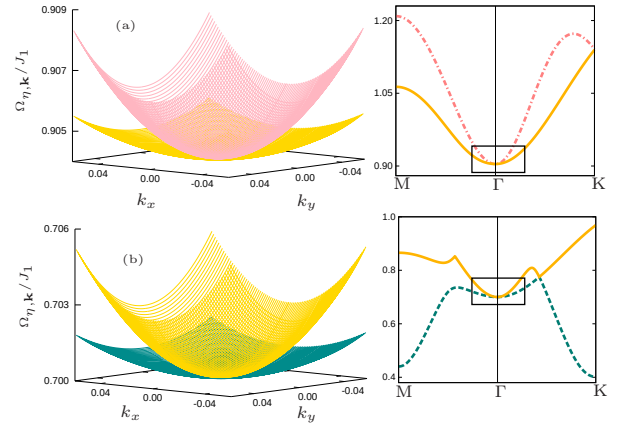


FIG. 9: Closer view of triplet excitations around the QBTPs (a) $J_2/J_1 = 0.30$ and (b) $J_2/J_1 = 0.45$.

circle) always appears at every vertex of the hexagonal BZ with the coordinates, $(0, \frac{4\pi}{9})$, $(0, -\frac{4\pi}{9})$, $(\frac{2\pi}{3\sqrt{3}}, \frac{2\pi}{9})$, $(-\frac{2\pi}{3\sqrt{3}}, \frac{2\pi}{9})$, $(\frac{2\pi}{3\sqrt{3}}, -\frac{2\pi}{9})$ and $(-\frac{2\pi}{3\sqrt{3}}, -\frac{2\pi}{9})$, for any values of J_2/J_1 . So, the QBTP (red square) always appears at the center of that (Γ point) when $J_2/J_1 < 0.337$. This situation is as shown in Fig 7(a) for $J_2/J_1 = 0.30$. When $J_2/J_1 = 0.337$, QBTP between upper bands (red square) at the center of BZ is replaced by the triple point (purple square), which is shown in Fig 7(b). Closer view of the energy dispersion in the vicinity of TBTP is shown in Fig 11 (a). Finally, the TBTP (purple square) is replaced by another QBTP between lower bands (blue square) at the center of BZ when $J_2/J_1 > 0.337$. The movable Dirac nodes appear symmetrically around the center of BZ as shown in Fig 7(c) for $J_2/J_1 = 0.45$.

Similarly in the region R_2 , 3D plots of the triplet excitations, $\Omega_{\eta,\mathbf{k}}/J_1$, covering the BZ, as well as along the one-dimensional pathway, have been shown in Fig 10 (a)-(e), for five different values of $J_2/J_1 =$ (a) 0.55, (b) 0.6007, (c) 0.65, (d) 0.68, (e) 0.75. The fixed Dirac node located at the K point is present as usual like before for any value of J_2/J_1 . The dispersion relation depicted in Fig 10 (a) is similar to that shown in Fig 7 (a), with the exception that the lowest band is flat in the region R_2 . The band gap is larger in this case. The emergence of TBTP point is noted like before, and this time it occurs for the value $J_2/J_1 = 0.6001$, which is shown by the purple square. Again it appears at the Γ point. A magnified

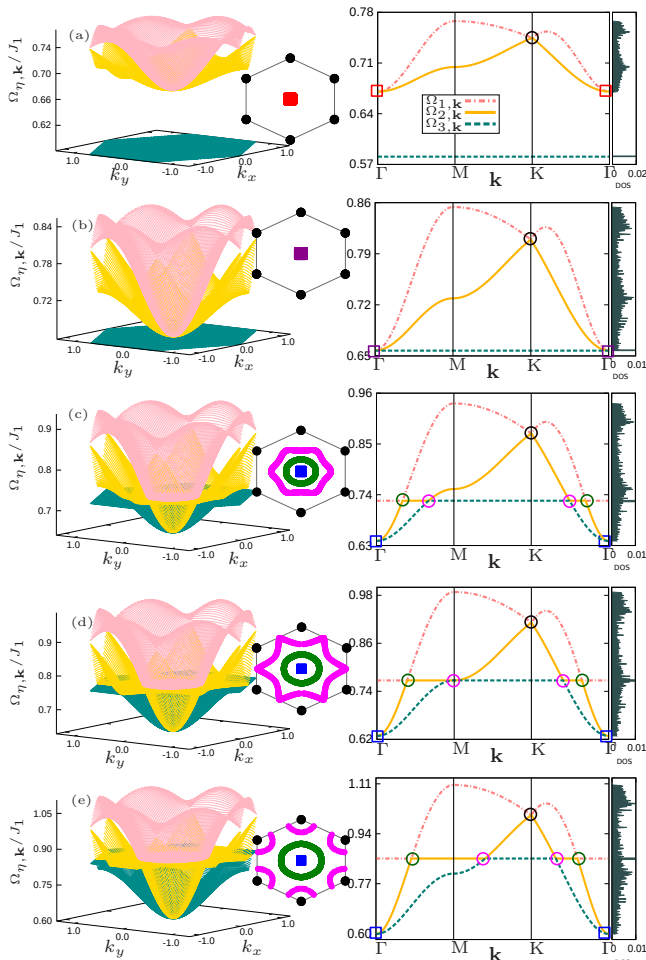


FIG. 10: Evolution of nodes and nodal lines in region R_2 with J_2/J_1 , $J_2/J_1 =$ (a) 0.55, (b) 0.6007, (c) 0.65, (d) 0.68, (e) 0.75.

view close to this touching point is shown in Fig 11 (b). In region R_2 , the lowest excitation till remains dispersionless, however, up to $J_2/J_1 = 0.61$. Thus, the dispersion relation presented in Fig 10 (b) can be compared to that in Fig 7 (b) in the same fashion.

The nature of dispersion relation for the region R_2 changes dramatically beyond the TBTP with the increase of J_2/J_1 . In this case, two DLNs appear where one between upper and another between lower two bands instead of the six pairs of Dirac nodes as found before in the region R_1 . Both the nodal lines are closed and appear at the same energy. Among the two associated bands, one is always flat for each of those two DLNs, which means that magnitude of DOS at this value of energy is extremely high. DLNs shift towards higher energies with the increase of J_2/J_1 .

Nodal line formed between the upper two bands is circular with the Γ point at its center, while that between the lower two bands is hexagonal and symmetric around the Γ point. In the beginning, both the DLNs are found in the immediate vicinity of Γ point. With the increase

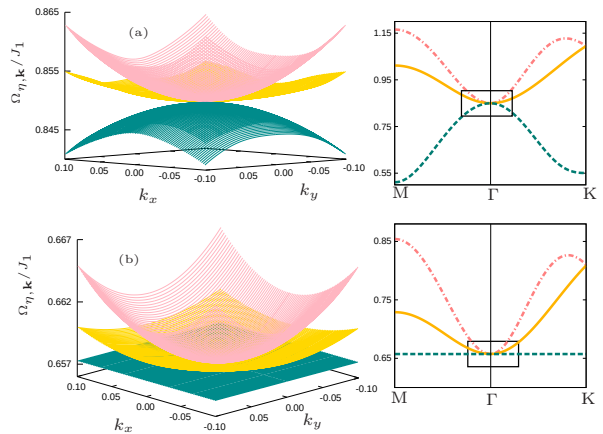


FIG. 11: Closer view of triplet excitations around the TBTPs for (a) $J_2/J_1 = 0.337$ and (b) $J_2/J_1 = 0.6001$.

of J_2/J_1 , both the nodal lines move away from the Γ point but with different fashions. The radius of the circular nodal line increases, while the hexagonal nodal line changes its shape and becomes K-centered circular one when J_2/J_1 crosses the value 0.68. The structural deformation in the later case takes place when $J_2/J_1 = 0.68$, or as soon as this nodal line touches the M point otherwise. Radius of this second circular nodal line decreases with the further increase of J_2/J_1 beyond 0.68. The evolution of two DLNs can be found in the Figs 10 (c) - (e). Fig 12 shows the magnified view of the two circular nodal lines centered around the K and Γ points, when $J_2/J_1 = 0.75$. Nonetheless, both the DLNs are always symmetric around the center of BZ (Γ point), which corresponds to the fact that they are topologically protected by the \mathcal{PT} -symmetry invariance of the system. Which means that these DLNs are of type $\text{II}^{20,21}$. However, all through the region, $0.61 \leq J_2/J_1 \leq 0.99$, a QBTP node between lower two bands (blue square) is found to present at the Γ point, which is again similar to the previous case. Fig 6 contains the kaleidoscope of distinct patterns of topological nodes formed within the BZ, over the whole parameter region, $0.11 \leq J_2/J_1 \leq 0.99$.

VII. TOPOLOGICAL PHASES

The system studied in terms of triplet operators is topologically trivial, since the Hamiltonian does not break the \mathcal{T} -symmetry. However, in this section, emergence of nontrivial topology in the R_1 region will be discussed in the presence of \mathcal{H}_P , which is $\text{SU}(2)$ invariant and breaks the \mathcal{T} -symmetry. It also satisfies an additional criterion, which states that the respective off-diagonal elements in the submatrices $X_{\mathbf{k}}$ and $Y_{\mathbf{k}}$ may be the same, barring at least one. This additional criterion is obtained empirically and found necessary for the non-

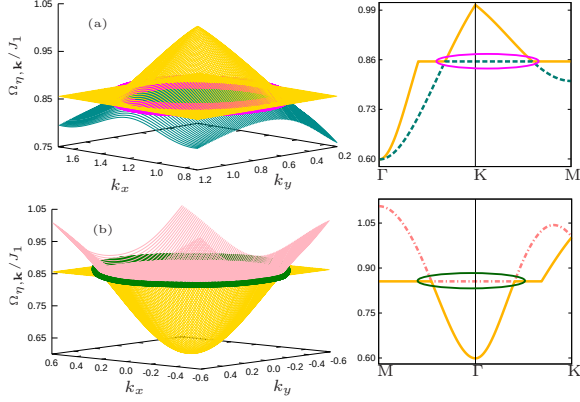


FIG. 12: Closer view of triplet excitations around the two circular nodal lines for $J_2/J_1 = 0.75$.

triviality in this case.

$$\mathcal{H}_P = \sum_{\mathbf{k}} iD_1 \left(t_{2^-, \mathbf{k}, \alpha}^\dagger t_{3^-, \mathbf{k}, \alpha} - t_{3^-, \mathbf{k}, \alpha}^\dagger t_{2^-, \mathbf{k}, \alpha} \right) + i \frac{D_2}{2} \left(t_{2^-, \mathbf{k}, \alpha}^\dagger t_{3^-, -\mathbf{k}, \alpha} - t_{2^-, -\mathbf{k}, \alpha} t_{3^-, \mathbf{k}, \alpha} \right).$$

The total Hamiltonian including \mathcal{H}_P is $SU(2)$ invariant, but breaks the \mathcal{T} -symmetry in this three-band system, since $H_{\mathbf{k}} \neq H_{-\mathbf{k}}^*$ ³⁸. The presence of \mathcal{H}_P lifts the degeneracy at the band touching points, at the same time, Berry curvature is deformed in such a way that non-zero Chern number emerges when $D_1 \neq D_2$. The condition, $D_1 \neq D_2$ implies one dissimilar term among the respective off-diagonal elements in the submatrices $X_{\mathbf{k}}$ and $Y_{\mathbf{k}}$, which ultimately satisfies the additional criterion in other words. Different topological phases appear with the variation of D 's in the region R_1 .

In order to draw a topological phase diagram, values of C for distinct triplet energy bands are obtained for every topological phase. The value of C of a particular band has been calculated by integrating the Berry curvature over the BZ,

$$C = \frac{1}{2\pi} \iint_{\text{BZ}} F(\mathbf{k}) dk_x dk_y, \quad (22)$$

where the Berry curvature of that band, $F(\mathbf{k})$, is expressed as, $A_\mu(\mathbf{k}) = \langle n(\mathbf{k}) | \partial_{k_\mu} | n(\mathbf{k}) \rangle$ as $F(\mathbf{k}) = \partial_{k_x} A_y(\mathbf{k}) - \partial_{k_y} A_x(\mathbf{k})$, and $|n(\mathbf{k})\rangle$ is the eigenvector of that particular triplet band in the $S_T^z = 0$ sector. However, the result will remain unchanged if the eigenvectors with $S_T^z = \pm$ sectors are taken into account instead, since the total Hamiltonian is still $SU(2)$ invariant. Value of C is obtained by evaluating the integral, Eq 22 numerically³⁹. The number of edge states is related with the non-zero Chern numbers which confirms the existence of nontrivial topological phase. This relation is governed by the BEC rule.

To calculate the edge state spectrum PBC imposed along the \hat{y} direction is removed. Which leaves a strip of

honeycomb lattice having N plaquettes along the \hat{y} direction. The system is still assumed infinitely long along the \hat{x} direction. A replica of this structure is shown in Fig 1 (f). By applying the Fourier transformation on the bosonic operators only along the \hat{x} direction, the Hamiltonian matrix of order $2N \times 2N$ for the resulting system has been obtained. Energies of triplet excitations for bulk-edge states are obtained by diagonalizing the Hamiltonian matrix numerically.

Bulk-edge dispersion relations for three distinct topological phases of the system have been shown in Fig 14 in the one-dimensional BZ. Energy dispersion obtained for $J_2/J_1 = 0.30$, $D_1/J_1 = 0.15$ and $D_2/J_1 = 0.5$ is shown in Fig 14 (a). The state of the system corresponds to topological phase with $C=(2, -2, 0)$. Topological phases with $C=(2, -4, 2)$ and $C=(0, -2, 2)$ appear when $D_2/J_1 = -0.7$ and -0.8 , respectively. Energy dispersion of those two topological phases are shown in Fig 14 (b) and (c), respectively. In every case, edge-state modes are found to appear in accordance to the BEC rule²⁷.

Total six distinct topological phases have been found in this system. The remaining three topological phases can be obtained in the following way. For a fixed J_2/J_1 , if a particular topological phase with $C=(n_1, n_2, n_3)$ appears at definite values of D 's, then, another topological phase with $C=(-n_1, -n_2, -n_3)$ must appear upon reversal of signs of D 's but keeping their values fixed. Hence Chern numbers are found to reverse their signs with the reversal of signs of D 's. This phenomenon is depicted in the topological phase diagrams of the system as shown in Figs 15 (a) and (b), where the values of D_1/J_1 are kept fixed at ± 0.15 , respectively.

Moreover, other topological phases apart from those six may appear with different choices of \mathcal{T} -symmetry breaking terms. But an arbitrary choice of \mathcal{H}_P may ultimately results in nonphysical complex eigenenergies for the following reasons. Eigenenergies are obtained via the bosonic Bogoliubov transformation where the product of I_B and $H_{\mathbf{k}}$ is being diagonalized instead of $H_{\mathbf{k}}$ alone, (Appendix C). This product is always a non-Hermitian matrix when the Hermitian \mathcal{H}_P with complex elements is added to the real $H_{\mathbf{k}}$. With some exception, non-Hermitian matrix generally leads to complex eigenvalues. In this study, values of D_1 and D_2 in \mathcal{H}_P are chosen in such a way that real eigenenergies are obtained. Surprisingly, no topological phase appears in the region R_2 by any choice of \mathcal{H}_P .

Most of the two-band systems like fermionic Haldane and Kitaev models formulated on the honeycomb lattice exhibit a unique topological phase, $C=\pm 1$, as well as the bosonic FM Heisenberg models including the NNN DMI term and the combination of NN Kitaev and SAI terms reveals the same phase in the presence of external magnetic field^{24,29,40,41}. Existence of that particular phase has been verified experimentally in the three different cases among four of them^{28,42,43}. In contrast, this three-band system exhibits multiple topological phases. In comparison to other magnetic systems, topological phases emerge in this case in the triplet excitations with

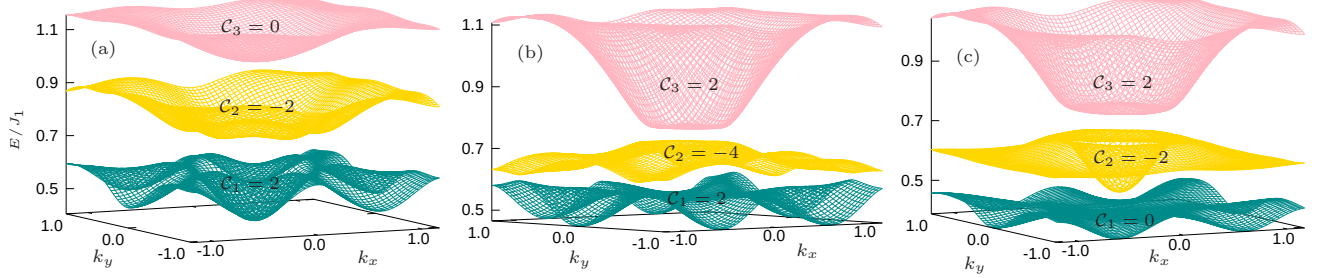


FIG. 13: The triplet dispersion relations after adding the \mathcal{H}_P term. Chern numbers of the respective bands are stated for three different topological phases.

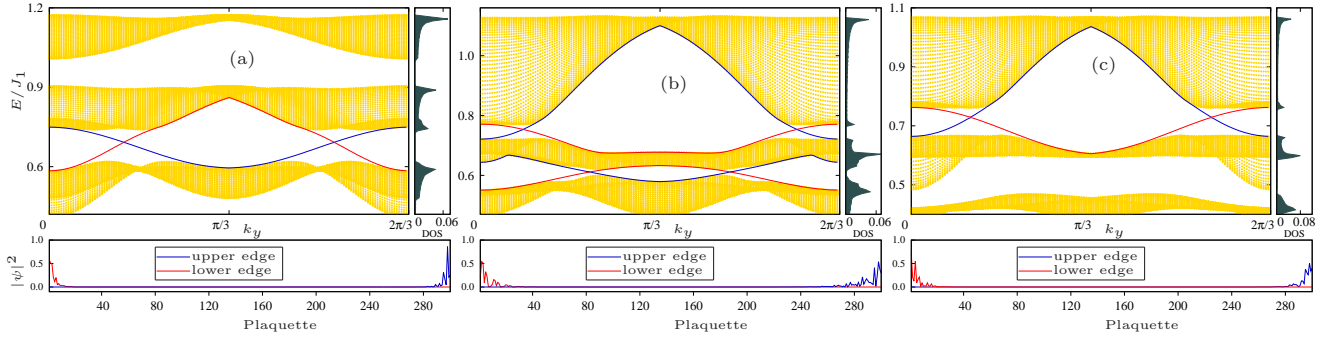


FIG. 14: Edge states of the plaquette honeycomb lattice. The side panel shows the DOS. The lower panel indicates variation of probability density of both edge modes with plaquette number at a fixed value of k_y .

respect to a spin-disordered ground state where the system is $SU(2)$ invariant. Further, coexistence of spin gap and topological phases is found in this model, while for the other bosonic systems topological phases are obtained in the absence of spin gap. However, in the Kitaev model, topological phase emerges on the spin-liquid ground state in the presence of spin gap when the magnetic field is non-zero⁴⁰.

In order to study the topological phase transition, value of thermal Hall conductance, κ_{xy} , has been computed. κ_{xy} of the system can be expressed in terms of $F(\mathbf{k})$ as⁴⁴,

$$\kappa_{xy}(T) = -\frac{k_B^2 T}{4\pi^2 \hbar} \sum_n \iint_{BZ} c(\rho_n(\mathbf{k})) F_n(\mathbf{k}) dk_x dk_y, \quad (23)$$

where n is the band index. T is the temperature, k_B is the Boltzmann constant and \hbar is the reduced Planck's constant. $F_n(\mathbf{k})$ is the Berry curvature of the n -th band. $c(x) = (1+x)(\ln \frac{1+x}{x})^2 - (\ln x)^2 - 2\text{Li}_2(-x)$, where $\text{Li}_2(z) = -\int_0^z du \frac{\ln(1-u)}{u}$, and $\rho_n(\mathbf{k})$ is the Bose-Einstein distribution function, *i.e.*, $\rho_n(\mathbf{k}) = 1/(e^{E_n^{\mathbf{k}}/k_B T} - 1)$. Value of $\kappa_{xy}(T)$ does not change at high temperature region and it is different for different topological phase. The variation of $\kappa_{xy}(T)$ with T for six different topological phases is shown in Fig 16.

The variation of κ_{xy} in the parameter space has been studied for fixed value of T to identify the transition

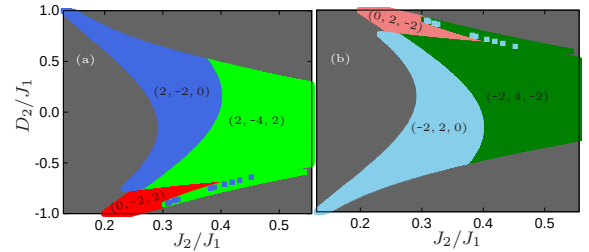


FIG. 15: Topological phase diagram for (a) $D_1/J_1 = 0.15$, (b) $D_1/J_1 = -0.15$.

among the various topological phases. When the system crosses topological phase boundary there is a discontinuity in κ_{xy} . Fig 17 (a) and (b) depict topological phase transition of the system with respect to D_2/J_1 for $D_1/J_1 = \pm 0.15$ at $J_2/J_1 = 0.30$.

VIII. DISCUSSION

In this investigation, emergence of a variety of multiple topological nodes is noted as well as a pair of DLNs and a flat band in the triplet dispersions of the three-band J_1 - J_2 AFM Heisenberg model on the honeycomb lattice on the basis of spin-disordered ground state throughout the whole frustrated parameter regime, $0 < J_2/J_1 < 1$.

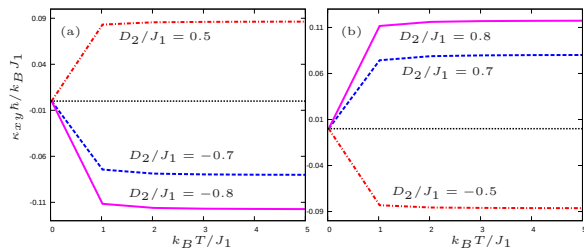


FIG. 16: Variation of κ_{xy} with T for (a) $D_1/J_1 = 0.15$, (b) $D_1/J_1 = -0.15$, when $J_2/J_1 = 0.30$.

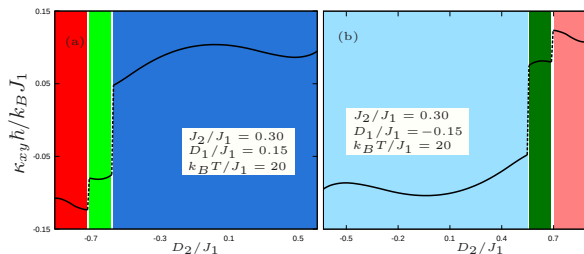


FIG. 17: Variation of κ_{xy} with D_2/J_1 when $k_B T / J_1 = 20$, $J_2/J_1 = 0.30$ and $D_1 = \pm 0.15$ in (a) and (b), respectively. Phase transition occurs at the points where κ_{xy} suffers a sudden jump.

The spin-disordered state is known as PVBS phase which actually prevails in the region $0.2 < J_2/J_1 < 0.4$, as a true ground state of the system. In order to estimate the ground state energy and spin gap, POT has been developed on the basis of a limited number of low energy exact eigenstates of a single J_1 - J_2 AFM Heisenberg hexagon, where all the exact eigenstates have been derived indeed. Expressions for the eigenvalues and eigenstates are given in the Appendix A. Two different PRVB states turn out as the ground states of a single hexagon plaquette in the two separate regions R_1 and R_2 , while it is doubly degenerate at the meeting point of the two regions. Thus, POT has been developed on the two regions separately based on the respective ground states. The values of ground state energy and spin gap obtained via POT is very close to the numerical estimations where PVBS phase persists. But beyond the region $0.2 < J_2/J_1 < 0.4$, POT overestimates the ground state energy. More accurate estimation is possible if higher energy eigenstates are taken into account in the POT, however, validity of POT is questionable in the spin-ordered regions as well. It must be noted at this point that although the ground state properties of this frustrated model has been studied before by using several methods⁴⁻¹⁵, but an extensive investigation on the topological properties is not yet undertaken.

Topological nodes in the forms of Dirac point, QBTP, and two different types of TBTPs are found to appear in this single model including a pair of degenerate DNLs in the triplet dispersion bands with respect to the spin-disordered ground state. Those nodes appear in this three-band system with the variation of J_2/J_1 . Thus, evolution of those point and line nodes in this system can be regarded as a result of variation of frustration within the system. One particular Dirac node among all of them is found to bear the reminiscence of honeycomb lattice, since its feature is similar to that appears before in graphene and Heisenberg honeycomb model in the collinear FM phase. Other nodes are tunable. Weyl nodes are found in the collinear FM phase of the Heisenberg honeycomb model when the NNNN interaction with strength above the critical value is taken into account²³. On the other hand, the lack of invariance in the collinear ground state under the \mathcal{M} -symmetry operation bars the emergence of Dirac node in the AFM case. All the point and line nodes in the triplet dispersions emerge with respect to the PVBS ground state with spin gap and when the system does not break the \mathcal{PT} -symmetry.

Additionally, the system hosts six distinct topological phases when a specific \mathcal{T} -symmetry breaking term is included. Incorporation of the symmetry breaking terms like, Zeeman, DMI, Kitaev and SAI, those are found to exist within the materials fail to induce nontriviality in this system. The reason behind this failure attributes to the fact that here POT is formulated in a direction where the system does not break the $SU(2)$ invariance in the every intermediate stage. Whereas, those symmetry breaking terms do not preserve $SU(2)$ but retain the $U(1)$ symmetry. Therefore, a modified version of POT on the basis of spin-singlet ground state requires which is valid for those systems where $SU(2)$ is lost but $U(1)$ symmetry is preserved. In the modified version of the POT, triple degeneracy of the every triplet dispersion will be broken leading to 18×18 Hamiltonian matrix, $H_{\mathbf{k}}$ in Eq 15, with the inclusion of other symmetry broken terms. So, the corresponding submatrices $X_{\mathbf{k}}$ and $Y_{\mathbf{k}}$ are of dimension 9×9 . In this situation, $H_{\mathbf{k}}$ must break the \mathcal{T} -symmetry but emergence of nontrivial topology may demand additional criteria.

IX. ACKNOWLEDGMENTS

We are grateful to Prof. P. Sindzingre for providing us the numerical data of ground state energy. MD acknowledges the UGC fellowship, No. 524067 (2014), India. AKG acknowledges a BRNS-sanctioned research project, No. 37(3)/14/16/2015, India.

* Electronic address: moumitadeb44@gmail.com

† Electronic address: asimkumar96@yahoo.com

¹ Y Onose, T Ideue, H Katsura, Y Shiomi, N Nagaosa and Y Tokura, Science, **329**, 297 (2010).

- ² S. Sachdev, Nat. Phys. **4**, 173 (2008).
- ³ G. Misguich and C. Lhuillier, Frustrated Spin Systems, edited by H. T. Diep (World Scientific, Singapore, 2004), p. 229.
- ⁴ A. F. Albuquerque, D. Schwandt, B. Hetényi, S. Capponi, M. Mambrini, and A. M. Läuchli, Phys. Rev. B **84**, 024406 (2011).
- ⁵ Z. Noorbakhsh, F. Shahbazi, S. A. Jafari and G. Baskaran, J. Phys. Soc. Jpn. **78**, 054701 (2009).
- ⁶ Z. Y. Meng, T. C. Lang, S. Wessel, F. F. Assaad, and A. Muramatsu, Nature (London) **464**, 847 (2010).
- ⁷ B. K. Clark, D. A. Abanin and S. L. Sondhi, Phys. Rev. Lett. **107**, 087204 (2011).
- ⁸ H. Mosadeq, F. Shahabazi and S. A. Jafari, J. Phys.: Condens. Matter **23**, 226006 (2011).
- ⁹ H. Zhang and C. A. Lamas, Phys. Rev. B **87**, 024415 (2013).
- ¹⁰ R. Ganesh, J. van den Brink, and S. Nishimoto, Phys. Rev. Lett. **110**, 127203 (2013).
- ¹¹ Z. Zhu, D. A. Huse, and S. R. White, Phys. Rev. Lett. **110**, 127205 (2013).
- ¹² S.-S. Gong, D. N. Sheng, O. I. Motrunich, and M. P. A. Fisher, Phys. Rev. B **88**, 165138 (2013).
- ¹³ R. F. Bishop, P. H. Y. Li, and C. E. Campbell, J. Phys.: Condens. Matter **25**, 306002 (2013).
- ¹⁴ J. Oitmaa and R. R. P. Singh, Phys. Rev. B **84**, 094424 (2011).
- ¹⁵ J. B. Fouet, P. Sindzingre and C. Lhuillier, Eur. Phys. J. B **20**, 241-245 (2001)
- ¹⁶ F. Ferrari and F. Becca, arXiv:1912.09310
- ¹⁷ R. Flint and P. A. Lee, Phys. Rev. Lett. **111**, 217201 (2013).
- ¹⁸ Y. Singh and P. Gagenwart, Phys. Rev. B **82**, 064412 (2010).
- ¹⁹ Y. D. Chong, X-G. Wen and M. Soljačić, Phys. Rev. B **77**, 235125 (2008).
- ²⁰ C. Fang, H. Weng, X. Dai and Z. Fang, Chin. Phys. B **25**, 117106 (2016).
- ²¹ A. Mook, J. Henk and I. Mertig, Phys. Rev. B **95**, 014418 (2017).
- ²² P. R. Wallace, Phys. Rev. **71**, 622 (1947).
- ²³ D. Boyko, A. V. Balatsky, and J. T. Haraldsen, Phys. Rev. B **97**, 014433 (2018).
- ²⁴ S A Owerre, J. Phys.: Condens. Matter **28**, 386001 (2016).
- ²⁵ S A Owerre, J. Phys.: Condens. Matter **30**, 28LT01 (2018).
- ²⁶ D J Thouless, M Kohomoto, P Nightingale and M den Nijs, Phys. Rev. Lett. **49**, 405 (1982).
- ²⁷ Y. Hatsugai, Phys. Rev. Lett. **71**, 3697 (1993).
- ²⁸ L. Chen, J. -H. Chung, B. Gao, T. Chen, M. B. Stone, A. I. Kolesnikov, Q. Huang, and P. Dai, Phys. Rev. X **8**, 041028 (2018).
- ²⁹ D. G. Joshi, Phys. Rev. B **98**, 060405(R) (2018).
- ³⁰ M. Deb and A. K. Ghosh, J. Phys.: Condens. Matter **31**, 345601 (2019).
- ³¹ S. Sachdev and R. N. Bhatt, Phys. Rev. B **41**, 9323 (1990).
- ³² M. E. Zhitomirsky and K. Ueda, Phys. Rev. B **54**, 9007 (1996).
- ³³ R. L. Doretto, Phys. Rev. B **89**, 104415 (2014).
- ³⁴ M. Deb and A. K. Ghosh, Eur. Phys. J. D **71**, 173 (2017).
- ³⁵ J. H. P. Colpa, Physica A **93**, 327 (1978).
- ³⁶ S. Paul and A. K. Ghosh, Condens. Matter Phys. **20**, 23701 (2017)
- ³⁷ P. Sindzingre, private communication.
- ³⁸ A. Sil and A. K. Ghosh, J. Phys.: Condens. Matter **32**, 025601 (2020).
- ³⁹ T. Fukui, Y Hatsugai and H Suzuki, J. Phys. Soc. Jpn. **74**, 1674 (2005).
- ⁴⁰ A Kitaev, Ann. Phys. **321**, 2 (2006).
- ⁴¹ F D M Haldane, Phys. Rev. Lett. **61**, 2015 (1988).
- ⁴² G. Yokzu *et. al.*, Nature **515**, 237 EP (2014).
- ⁴³ T. Yokoi *et. al.*, arXiv:2001.01899
- ⁴⁴ R. Matsumoto and S. Murakami, Phys. Rev. Lett. **106**, 197202 (2011).

Appendix A: ENERGY EIGENVALUES AND EIGENSTATES OF THE HEISENBERG HEXAGON

In this appendix, expressions of all the eigenvectors ($|\nu\rangle$) and eigenvalues (E_ν) of the Heisenberg Hamiltonian for a single hexagonal plaquette (Eq 1) are given by solving the eigenvalue equation, $H^\circ|\nu\rangle = E_\nu|\nu\rangle$. H° possesses the symmetry of a regular hexagon, which is studied in terms of a group of 12 elements, known as dihedral group D_6 . D_6 is composed of six rotations, \hat{R}_n and six reflections, \hat{M}_n , $n = 1, 2, 3, 4, 5, 6$. \hat{R}_n be the successive \hat{R} operation by n times, where \hat{R} implies the rotation by $\pi/3$ about the center of the hexagon, as depicted in Fig 1 (e). Six different mirror planes for \hat{M}_n operations are shown by dashed lines in Fig 1 (f).

For the counter clockwise rotation by $\pi/3$, the rotational operator, \hat{R} , can be defined as $\hat{R}|S_1S_2S_3S_4S_5S_6\rangle = |S_2S_3S_4S_5S_6S_1\rangle$, where $|S_1S_2S_3S_4S_5S_6\rangle = |S_1^z\rangle \otimes |S_2^z\rangle \otimes |S_3^z\rangle \otimes |S_4^z\rangle \otimes |S_5^z\rangle \otimes |S_6^z\rangle$, in which $|S_n^z\rangle$ is the spin state at the n -th vertex. Obviously \hat{R}_6 is the identity operation which leaves any state unaltered. Each eigenstate of the Hamiltonian, $|\nu\rangle$ has a definite rotational property, which can be described in terms of an eigenvalue equation, like $\hat{R}_p|\nu\rangle = \lambda_r|\nu\rangle$, where λ_r be the eigenvalue of the rotational operator \hat{R}_p . The value of p corresponds to the minimum number \hat{R} operations on a definite state unless λ_r assumes the value either $+1$ or -1 . Obviously, for the same state λ_r is always $+1$ for $2p$ number of \hat{R} operations. The states with $\lambda_r = +1$ have even parity (symmetric) while those with $\lambda_r = -1$ have odd parity (antisymmetric). It is found that, every eigenstate has definite values of both p and λ_r , and subsequently has definite parity. 36 states have even parity while the remaining 28 states have odd parity. Values of p and λ_r for all eigenstates are shown in the Table I. It is observed that p takes up either 1 or 3 and never takes up 2, 4 and 5. For Ψ_{RVB} , $\lambda_r = -1$ and $p = 1$, while, for Ψ'_{RVB} , $\lambda_r = 1$ and $p = 1$. Thus, Ψ'_{RVB} does not change sign under any number of \hat{R} operations, while Ψ_{RVB} changes sign for odd numbers of \hat{R} operations. So, Ψ_{RVB} is antisymmetric, whereas, Ψ'_{RVB} is symmetric under the rotation by the angle $\pi/3$.

Similarly, the effect of reflections of the eigenstates can be studied in terms of an eigenvalue equation $\hat{M}_n|\nu\rangle =$

$\lambda_{M_n}|\nu\rangle$. Obviously, \hat{M}_n^2 is the identity operation which on the otherhand fixes the values of λ_{M_n} to be ± 1 in this case. The operations \hat{M}_n are defined as

$$\begin{aligned}\hat{M}_1 |S_1 S_2 S_3 S_4 S_5 S_6\rangle &= |S_1 S_6 S_5 S_4 S_3 S_2\rangle, & \hat{M}_2 |S_1 S_2 S_3 S_4 S_5 S_6\rangle &= |S_3 S_2 S_1 S_6 S_5 S_4\rangle, \\ \hat{M}_3 |S_1 S_2 S_3 S_4 S_5 S_6\rangle &= |S_5 S_4 S_3 S_2 S_1 S_6\rangle, & \hat{M}_4 |S_1 S_2 S_3 S_4 S_5 S_6\rangle &= |S_6 S_5 S_4 S_3 S_2 S_1\rangle, \\ \hat{M}_5 |S_1 S_2 S_3 S_4 S_5 S_6\rangle &= |S_2 S_1 S_6 S_5 S_4 S_3\rangle, & \hat{M}_6 |S_1 S_2 S_3 S_4 S_5 S_6\rangle &= |S_4 S_3 S_2 S_1 S_6 S_5\rangle.\end{aligned}\tag{A1}$$

TABLE I: Energy and other eigenvalues of the eigenstates of spin-1/2 Heisenberg hexagon

$S_{\mathbf{T}}$	$S_{\mathbf{T}}^z$	Energy eigenvalues	λ_r	p	λ_{M_1}	λ_{M_2}	λ_{M_3}	λ_{M_4}	λ_{M_5}	λ_{M_6}
0	0	$E_{s_{1\pm}} = -J_1 \pm \frac{1}{2}d_s$	-1	1	1	1	1	-1	-1	-1
0	0	$E_{s_2} = -\frac{3}{2}(J_1 + J_2)$	1	1	-1	-1	-1	-1	-1	-1
0	0	$E_{s_3} = -\frac{1}{2}(J_1 + 3J_2)$	-1	3	1					-1
0	0	$E_{s_4} = -\frac{1}{2}(J_1 + 3J_2)$	-1	3	-1					1
1		$E_{t_{1\pm,\alpha}} = -J_1 \pm \frac{1}{2}d_{t_1}$	1	1	1	1	1	1	1	1
1	0	$E_{t_{1\pm,z}} = -J_1 \pm \frac{1}{2}d_{t_1}$	1	1	1	1	1	1	1	1
1		$E_{t_{2\pm,\alpha}} = -\frac{1}{4}(J_1 + 3J_2 \mp d_{t_2})$	1	3	1					1
1	0	$E_{t_{2\pm,z}} = -\frac{1}{4}(J_1 + 3J_2 \mp d_{t_2})$	1	3	1					1
1		$E_{t_{3\pm,\alpha}} = -\frac{1}{4}(J_1 + 3J_2 \mp d_{t_2})$	1	3	-1					-1
1	0	$E_{t_{3\pm,z}} = -\frac{1}{4}(J_1 + 3J_2 \mp d_{t_2})$	1	3	-1					-1
1		$E_{t_{4,\alpha}} = -J_1$	-1	3	-1					1
1	0	$E_{t_{4,z}} = -J_1$	-1	3			-1		1	
1		$E_{t_{5,\alpha}} = -J_1$	-1	3	1					-1
1	0	$E_{t_{5,z}} = -J_1$	-1	3			1		-1	
1		$E_{t_{6,\alpha}} = \frac{1}{2}(J_1 - 3J_2)$	-1	1	-1	-1	-1	1	1	1
1	0	$E_{t_{6,z}} = \frac{1}{2}(J_1 - 3J_2)$	-1	1	-1	-1	-1	1	1	1
2		$E_{q_{1,1\pm}} = J_1$	-1	3		-1		1		
2		$E_{q_{1,\alpha}} = J_1$	-1	3			-1		1	
2	0	$E_{q_{1,z}} = J_1$	-1	3	-1					1
2		$E_{q_{2,1\pm}} = J_1$	-1	3		1		-1		
2		$E_{q_{2,\alpha}} = J_1$	-1	3			1		-1	
2	0	$E_{q_{2,z}} = J_1$	-1	3	1					-1
2		$E_{q_{3,1\pm}} = 0$	1	3			1		1	
2		$E_{q_{3,\alpha}} = 0$	1	3	1					1
2	0	$E_{q_{3,z}} = 0$	1	3	1					1
2		$E_{q_{4,1\pm}} = 0$	1	3			-1		-1	
2		$E_{q_{4,\alpha}} = 0$	1	3	-1					-1
2	0	$E_{q_{4,z}} = 0$	1	3	-1					-1
2		$E_{q_{5,1\pm}} = \frac{1}{2}(-J_1 + 3J_2)$	-1	1	1	1	1	-1	-1	-1
2		$E_{q_{5,\alpha}} = \frac{1}{2}(-J_1 + 3J_2)$	-1	1	1	1	1	-1	-1	-1
2	0	$E_{q_{5,z}} = \frac{1}{2}(-J_1 + 3J_2)$	-1	1	1	1	1	-1	-1	-1
3		$E_{h_{1\pm}} = \frac{3}{2}(J_1 + J_2)$	1	1	1	1	1	1	1	1
3		$E_{h_{2\pm}} = \frac{3}{2}(J_1 + J_2)$	1	1	1	1	1	1	1	1
3		$E_{h_\alpha} = \frac{3}{2}(J_1 + J_2)$	1	1	1	1	1	1	1	1
3	0	$E_{h_z} = \frac{3}{2}(J_1 + J_2)$	1	1	1	1	1	1	1	1

where, $d_s = \sqrt{13J_1^2 + 9J_2^2 - 18J_1J_2}$, $d_{t_1} = \sqrt{5J_1^2 + 9J_2^2 - 10J_1J_2}$, $d_{t_2} = \sqrt{17J_1^2 + 9J_2^2 - 10J_1J_2}$.

All energy eigenvalues along with the corresponding eigenvalues of the group operations on the eigenstates are listed in the Table I. Here, the energy eigenstates of a definite energy value are constructed in such a fashion that they

are the eigenstates of S_T^z only when the corresponding eigenvalue is zero. Otherwise they are expressed as a linear combinations of eigenstates of S_T^z with eigenvalues $\pm 1, \pm 2, \pm 3$, separately when $S_T > 0$. As a result, eigenvalue of S_T^z (second column of Table I) is not defined for every energy eigenstate. λ_{M_n} does not always have definite value. The energy eigenstates are expressed in this way because of the fact that these forms are found useful to construct the spin operators in the plaquette operator theory as presented in the Appendix B. However, energy eigenstates with definite values of S_T^z are available for a more general Heisenberg hexagon in the article³⁴.

To write down all the eigenstates following notations have been used.

$$\begin{aligned}
|\psi_n^3\rangle &= T^{n-1} |3\rangle (n = 1), |3\rangle = |\uparrow\uparrow\uparrow\uparrow\uparrow\rangle, \\
|\psi_n^2\rangle &= T^{n-1} |2\rangle (n = 1, 2, 3, 4, 5, 6), |2\rangle = |\uparrow\uparrow\uparrow\uparrow\downarrow\rangle, \\
|\psi_n^1\rangle_0 &= T^{n-1} |1\rangle_0 (n = 1, 2, 3, 4, 5, 6), |1\rangle_0 = |\uparrow\uparrow\uparrow\downarrow\uparrow\rangle, \\
|\psi_n^1\rangle_1 &= T^{n-1} |1\rangle_1 (n = 1, 2, 3, 4, 5, 6), |1\rangle_1 = |\downarrow\uparrow\uparrow\downarrow\uparrow\rangle, \\
|\psi_n^1\rangle_2 &= T^{n-1} |1\rangle_2 (n = 1, 2, 3), |1\rangle_2 = |\downarrow\uparrow\uparrow\downarrow\uparrow\rangle, \\
|\psi_n^0\rangle_0 &= T^{n-1} |0\rangle_0 (n = 1, 2, 3, 4, 5, 6), |0\rangle_0 = |\uparrow\uparrow\uparrow\downarrow\downarrow\rangle, \\
|\psi_n^0\rangle_1 &= T^{n-1} |0\rangle_1 (n = 1, 2, 3, 4, 5, 6), |0\rangle_1 = |\uparrow\uparrow\downarrow\downarrow\uparrow\rangle, \\
|\psi_n^0\rangle_2 &= T^{n-1} |0\rangle_2 (n = 1, 2, 3, 4, 5, 6), |0\rangle_2 = |\uparrow\downarrow\uparrow\downarrow\uparrow\rangle, \\
|\psi_n^0\rangle_3 &= T^{n-1} |0\rangle_3 (n = 1, 2), |0\rangle_3 = |\uparrow\downarrow\uparrow\downarrow\uparrow\rangle, \\
|\psi_n^{-1}\rangle_0 &= T^{n-1} |-1\rangle_0 (n = 1, 2, 3, 4, 5, 6), |-1\rangle_0 = |\downarrow\downarrow\uparrow\uparrow\downarrow\rangle, \\
|\psi_n^{-1}\rangle_1 &= T^{n-1} |-1\rangle_1 (n = 1, 2, 3, 4, 5, 6), |-1\rangle_1 = |\uparrow\downarrow\downarrow\uparrow\downarrow\rangle, \\
|\psi_n^{-1}\rangle_2 &= T^{n-1} |-1\rangle_2 (n = 1, 2, 3), |-1\rangle_2 = |\uparrow\downarrow\uparrow\downarrow\downarrow\rangle, \\
|\psi_n^{-2}\rangle &= T^{n-1} |-2\rangle (n = 1, 2, 3, 4, 5, 6), |-2\rangle = |\downarrow\downarrow\downarrow\downarrow\uparrow\rangle, \\
|\psi_n^{-3}\rangle &= T^{n-1} |-3\rangle (n = 1), |-3\rangle = |\downarrow\downarrow\downarrow\downarrow\downarrow\rangle.
\end{aligned} \tag{A2}$$

Here T is a unitary cyclic right shift operator. $T|abcdef\rangle = |fabcde\rangle$ where $|abcdef\rangle = |a\rangle \otimes |b\rangle \otimes |c\rangle \otimes |d\rangle \otimes |e\rangle \otimes |f\rangle$. All the energy eigenstates have been listed below.

$$\begin{aligned}
|s_{1\pm}\rangle &= \frac{1}{\mu_{s_{1\pm}} \sqrt{12}} \left(\sum_{n=1,6} (-1)^{n-1} (\sqrt{2} C_{s_{1\pm},3} |\psi_n^0\rangle_0 + C_{s_{1\pm},2} (|\psi_n^0\rangle_1 + |\psi_n^0\rangle_2)) + \sqrt{6} C_{s_{1\pm},1} \sum_{n=1}^2 (-1)^{n-1} |\psi_n^0\rangle_3 \right) \\
|s_2\rangle &= \frac{1}{\sqrt{12}} \left(\sum_{n=1}^6 (|\psi_n^0\rangle_2 - |\psi_n^0\rangle_1) \right) \\
|s_3\rangle &= \frac{1}{2} \left(\sum_{n=3,6} (-1)^n |\psi_n^0\rangle_0 + \sum_{n=1,4} (-1)^n (|\psi_n^0\rangle_1 + |\psi_n^0\rangle_2) \right) + \frac{1}{6} \sum_{n=1}^6 (-1)^{n-1} (|\psi_n^0\rangle_0 + |\psi_n^0\rangle_1 + |\psi_n^0\rangle_2) \\
|s_4\rangle &= \frac{1}{\sqrt{12}} \left(\sum_{n=1}^2 |\psi_n^0\rangle_0 - \sum_{n=4}^5 |\psi_n^0\rangle_0 + \sum_{n=5}^6 (|\psi_n^0\rangle_1 + |\psi_n^0\rangle_2) - \sum_{n=2}^3 (|\psi_n^0\rangle_1 + |\psi_n^0\rangle_2) \right) \\
|t_{1\pm,\alpha}\rangle &= \frac{\lambda_\alpha}{\mu_{t_{1\pm}} \sqrt{12}} \left(\sum_{n=1}^6 (C_{t_{1\pm},1}^\alpha (|\psi_n^1\rangle_0 \mp |\psi_n^{-1}\rangle_0) + C_{t_{1\pm},2}^\alpha (|\psi_n^1\rangle_1 \mp |\psi_n^{-1}\rangle_1)) + \sqrt{2} C_{t_{1\pm},3}^\alpha \sum_{n=1}^3 (|\psi_n^1\rangle_2 \mp |\psi_n^{-1}\rangle_2) \right) \\
|t_{1\pm,z}\rangle &= \frac{1}{\mu_{t_{1\pm}}^z \sqrt{12}} \left(\sum_{n=1}^6 (\sqrt{2} C_{t_{1\pm},3}^z |\psi_n^0\rangle_0 + C_{t_{1\pm},1}^z (|\psi_n^0\rangle_1 + |\psi_n^0\rangle_2)) + \sqrt{6} C_{t_{1\pm},2}^z \sum_{n=1}^2 |\psi_n^0\rangle_3 \right) \\
|t_{2\pm,\alpha}\rangle &= \frac{\lambda_\alpha}{\mu_{t_{2\pm}} \sqrt{24}} \left(3 \sum_{n=2,5} (C_{t_{2\pm},1}^\alpha (|\psi_n^1\rangle_0 \mp |\psi_n^{-1}\rangle_0) + C_{t_{2\pm},2}^\alpha (|\psi_n^1\rangle_1 \mp |\psi_n^{-1}\rangle_1)) - \sum_{n=1}^6 (C_{t_{2\pm},1}^\alpha (|\psi_n^1\rangle_0 \mp |\psi_n^{-1}\rangle_0) \right. \\
&\quad \left. + C_{t_{2\pm},2}^\alpha (|\psi_n^1\rangle_1 \mp |\psi_n^{-1}\rangle_1)) \right) + \frac{\lambda_\alpha}{\mu_{t_{2\pm}} \sqrt{12}} C_{t_{2\pm},3}^\alpha \left(2 (|1\rangle_2 \mp |-1\rangle_2) - \sum_{n=2}^3 (|\psi_n^1\rangle_2 \mp |\psi_n^{-1}\rangle_2) \right) \\
|t_{2\pm,z}\rangle &= \frac{C_{t_{2\pm},1}^z}{\mu_{t_{2\pm}}^z \sqrt{24}} \left(3 \sum_{n=1,4} (|\psi_n^0\rangle_1 + |\psi_n^0\rangle_2) - \sum_{n=1}^6 (|\psi_n^0\rangle_1 + |\psi_n^0\rangle_2) \right) + \frac{C_{t_{2\pm},2}^z}{\mu_{t_{2\pm}}^z \sqrt{12}} \left(3 \sum_{n=3,6} |\psi_n^0\rangle_0 - \sum_{n=1}^6 |\psi_n^0\rangle_0 \right)
\end{aligned}$$

$$\begin{aligned}
|t_{3^\pm, \alpha}\rangle &= \frac{\lambda_\alpha}{\sqrt{8}\mu_{t_{3^\pm}^\alpha}} \left(\sum_{n=1,4} \left(C_{t_{3^\pm,1}^\alpha} (|\psi_n^1\rangle_0 \mp |\psi_n^{-1}\rangle_0) + C_{t_{3^\pm,2}^\alpha} (|\psi_n^1\rangle_1 \mp |\psi_n^{-1}\rangle_1) \right) \right. \\
&\quad \left. - \sum_{n=3,6} \left(C_{t_{3^\pm,1}^\alpha} (|\psi_n^1\rangle_0 \mp |\psi_n^{-1}\rangle_0) + C_{t_{3^\pm,2}^\alpha} (|\psi_n^1\rangle_1 \mp |\psi_n^{-1}\rangle_1) \right) \right) + \frac{\lambda_\alpha}{2\mu_{t_{3^\pm}^\alpha}} C_{t_{3^\pm,3}^\alpha} \sum_{n=2}^3 (-1)^{n-1} (|\psi_n^1\rangle_2 \mp |\psi_n^{-1}\rangle_2) \\
|t_{3^\pm, z}\rangle &= \frac{C_{t_{3^\pm,1}^z}}{\mu_{t_{3^\pm}^z} \sqrt{8}} \left(\sum_{n=3,6} (|\psi_n^0\rangle_1 + |\psi_n^0\rangle_2) - \sum_{n=2,5} (|\psi_n^0\rangle_1 + |\psi_n^0\rangle_2) \right) + \frac{C_{t_{3^\pm,2}^z}}{2\mu_{t_{3^\pm}^z}} \left(\sum_{n=2,5} |\psi_n^0\rangle_0 - \sum_{n=1,4} |\psi_n^0\rangle_0 \right) \\
|t_{4, \alpha}\rangle &= \frac{\lambda_\alpha}{\sqrt{96}} \left(\sum_{n=1}^6 (-1)^n (|\psi_n^1\rangle_0 \mp |\psi_n^{-1}\rangle_0) + 3 \sum_{n=1,4}^6 (-1)^{n-1} (|\psi_n^1\rangle_0 \mp |\psi_n^{-1}\rangle_0) \right. \\
&\quad \left. + 3 \sum_{n=2}^3 (|\psi_n^1\rangle_1 \mp |\psi_n^{-1}\rangle_1) - 3 \sum_{n=5}^6 (|\psi_n^1\rangle_1 \mp |\psi_n^{-1}\rangle_1) \right) \\
|t_{4, z}\rangle &= \frac{1}{\sqrt{24}} \left(\sum_{n=1}^6 (-1)^n (|\psi_n^0\rangle_1 - |\psi_n^0\rangle_2) + 3 \sum_{n=3,6}^6 (-1)^{n-1} (|\psi_n^0\rangle_1 - |\psi_n^0\rangle_2) \right) \\
|t_{5, \alpha}\rangle &= \frac{\lambda_\alpha}{4\sqrt{2}} \left(\sum_{n=2}^3 (|\psi_n^1\rangle_0 \mp |\psi_n^{-1}\rangle_0) - \sum_{n=5}^6 (|\psi_n^1\rangle_0 \mp |\psi_n^{-1}\rangle_0) + \sum_{n=1}^6 (-1)^{n-1} (|\psi_n^1\rangle_1 \mp |\psi_n^{-1}\rangle_1) \right. \\
&\quad \left. + 3 \sum_{n=1,4}^3 (-1)^n (|\psi_n^1\rangle_1 \mp |\psi_n^{-1}\rangle_1) \right) \\
|t_{5, z}\rangle &= \frac{1}{\sqrt{8}} \left(\sum_{n=1,2}^3 (-1)^n (|\psi_n^0\rangle_2 - |\psi_n^0\rangle_1) + \sum_{n=4,5}^6 (-1)^{n-1} (|\psi_n^0\rangle_1 - |\psi_n^0\rangle_2) \right) \\
|t_{6, \alpha}\rangle &= \frac{\lambda_\alpha}{\sqrt{12}} \sum_{n=1}^6 (-1)^n (|\psi_n^1\rangle_0 \mp |\psi_n^{-1}\rangle_0) \\
|t_{6, z}\rangle &= \frac{1}{\sqrt{12}} \left(\sum_{n=1}^6 (-1)^{n-1} (|\psi_n^0\rangle_1 - |\psi_n^0\rangle_2) \right) \\
|q_{1,1^\pm}\rangle &= \frac{1}{2\sqrt{2}} \left(\sum_{n=1}^2 (|\psi_n^2\rangle \pm |\psi_n^{-2}\rangle) - \sum_{n=4}^5 (|\psi_n^2\rangle \pm |\psi_n^{-2}\rangle) \right) \\
|q_{1, \alpha}\rangle &= \frac{\lambda_\alpha}{4\sqrt{2}} \left(\sum_{n=1}^6 (-1)^{n-1} (|\psi_n^1\rangle_0 \mp |\psi_n^{-1}\rangle_0) + 3 \sum_{n=1,4}^3 (-1)^n (|\psi_n^1\rangle_0 \mp |\psi_n^{-1}\rangle_0) \right. \\
&\quad \left. + \sum_{n=2}^3 (|\psi_n^1\rangle_1 \mp |\psi_n^{-1}\rangle_1) - \sum_{n=5}^6 (|\psi_n^1\rangle_1 \mp |\psi_n^{-1}\rangle_1) \right) \\
|q_{1, z}\rangle &= \frac{1}{\sqrt{24}} \left(2 \sum_{n=1}^2 |\psi_n^0\rangle_0 - 2 \sum_{n=4}^5 |\psi_n^0\rangle_0 + \sum_{n=2}^3 (|\psi_n^0\rangle_1 + |\psi_n^0\rangle_2) - \sum_{n=5}^6 (|\psi_n^0\rangle_1 + |\psi_n^0\rangle_2) \right) \\
|q_{2,1^\pm}\rangle &= \frac{1}{\sqrt{24}} \left(\sum_{n=1}^6 (-1)^{n-1} (|\psi_n^2\rangle \pm |\psi_n^{-2}\rangle) + 3 \sum_{n=3,6}^6 (-1)^n (|\psi_n^2\rangle \pm |\psi_n^{-2}\rangle) \right) \\
|q_{2, \alpha}\rangle &= \frac{\lambda_\alpha}{\sqrt{96}} \left(3 \sum_{n=2}^3 (|\psi_n^1\rangle_0 \mp |\psi_n^{-1}\rangle_0) - 3 \sum_{n=5}^6 (|\psi_n^1\rangle_0 \mp |\psi_n^{-1}\rangle_0) + \sum_{n=1}^6 (-1)^n (|\psi_n^1\rangle_1 \mp |\psi_n^{-1}\rangle_1) \right. \\
&\quad \left. + 3 \sum_{n=1,4}^3 (-1)^{n-1} (|\psi_n^1\rangle_1 \mp |\psi_n^{-1}\rangle_1) \right) \\
|q_{2, z}\rangle &= \frac{1}{\sqrt{72}} \left(6 \sum_{n=3,6}^6 (-1)^n |\psi_n^0\rangle_0 + 3 \sum_{n=1,4}^3 (-1)^{n-1} (|\psi_n^0\rangle_1 + |\psi_n^0\rangle_2) + \sum_{n=1}^6 (-1)^n (|\psi_n^0\rangle_1 + |\psi_n^0\rangle_2 - 2|\psi_n^0\rangle_0) \right) \\
|q_{3,1^\pm}\rangle &= \frac{1}{\sqrt{24}} \left(3 \sum_{n=1,4}^3 (|\psi_n^2\rangle \pm |\psi_n^{-2}\rangle) - \sum_{n=1}^6 (|\psi_n^2\rangle \pm |\psi_n^{-2}\rangle) \right) \\
|q_{3, \alpha}\rangle &= \frac{\lambda_\alpha}{\sqrt{96}} \left(3 \sum_{n=2,5}^3 ((|\psi_n^1\rangle_0 \mp |\psi_n^{-1}\rangle_0) + (|\psi_n^1\rangle_1 \mp |\psi_n^{-1}\rangle_1)) - \sum_{n=1}^6 ((|\psi_n^1\rangle_0 \mp |\psi_n^{-1}\rangle_0) \right. \\
&\quad \left. + (|\psi_n^1\rangle_1 \mp |\psi_n^{-1}\rangle_1)) + 2 \sum_{n=2}^3 (|\psi_n^1\rangle_2 \mp |\psi_n^{-1}\rangle_2) - 4 (|1\rangle_2 \mp |-1\rangle_2) \right)
\end{aligned}$$

$$\begin{aligned}
|q_{3,z}\rangle &= \frac{1}{\sqrt{8}} \left(\sum_{n=2,5} (|\psi_n^0\rangle_2 - |\psi_n^0\rangle_1) + \sum_{n=3,6} (|\psi_n^0\rangle_1 - |\psi_n^0\rangle_2) \right) \\
|q_{4,1\pm}\rangle &= \frac{1}{2\sqrt{2}} \left(\sum_{n=3,6} (|\psi_n^2\rangle \pm |\psi_n^{-2}\rangle) - \sum_{n=2,5} (|\psi_n^2\rangle \pm |\psi_n^{-2}\rangle) \right) \\
|q_{4,\alpha}\rangle &= \frac{\lambda_\alpha}{4\sqrt{2}} \left(\sum_{n=1,4} ((|\psi_n^1\rangle_0 \mp |\psi_n^{-1}\rangle_0) + (|\psi_n^1\rangle_1 \mp |\psi_n^{-1}\rangle_1)) - \sum_{n=3,6} ((|\psi_n^1\rangle_0 \mp |\psi_n^{-1}\rangle_0) \right. \\
&\quad \left. + (|\psi_n^1\rangle_1 \mp |\psi_n^{-1}\rangle_1)) + 2 \sum_{n=2}^3 (-1)^n (|\psi_n^1\rangle_2 \pm |\psi_n^{-1}\rangle_2) \right) \\
|q_{4,z}\rangle &= \frac{1}{\sqrt{24}} \left(3 \sum_{n=1,4} (|\psi_n^0\rangle_1 - |\psi_n^0\rangle_2) + \sum_{n=1}^6 (|\psi_n^0\rangle_2 - |\psi_n^0\rangle_1) \right) \\
|q_{5,1\pm}\rangle &= \frac{1}{\sqrt{12}} \left(\sum_{n=1}^6 (-1)^{n-1} (|\psi_n^2\rangle \pm |\psi_n^{-2}\rangle) \right) \\
|q_{5,\alpha}\rangle &= \frac{\lambda_\alpha}{\sqrt{12}} \left(\sum_{n=1}^6 (-1)^{n-1} (|\psi_n^1\rangle_1 \mp |\psi_n^{-1}\rangle_1) \right) \\
|q_{5,z}\rangle &= \frac{1}{6} \left(\sum_{n=1}^6 (-1)^{n-1} (|\psi_n^0\rangle_0 + |\psi_n^0\rangle_1 + |\psi_n^0\rangle_2) + 3 \sum_{n=1}^2 (-1)^{n-1} |\psi_n^0\rangle_3 \right) \\
|h_{1\pm}\rangle &= \frac{1}{\sqrt{2}} (|\psi_n^3\rangle \pm |\psi_n^{-3}\rangle) \\
|h_{2\pm}\rangle &= \frac{1}{\sqrt{12}} \sum_{n=1}^6 (|\psi_n^2\rangle \pm |\psi_n^{-2}\rangle) \\
|h_\alpha\rangle &= \frac{\lambda_\alpha}{\sqrt{30}} \left(\sum_{n=1}^6 ((|\psi_n^1\rangle_0 \mp |\psi_n^{-1}\rangle_0) + (|\psi_n^1\rangle_1 \mp |\psi_n^{-1}\rangle_1)) + \sum_{n=1}^3 (|\psi_n^1\rangle_2 \mp |\psi_n^{-1}\rangle_2) \right) \\
|h_z\rangle &= \frac{1}{\sqrt{20}} \left(\sum_{n=1}^6 (|\psi_n^0\rangle_0 + |\psi_n^0\rangle_1 + |\psi_n^0\rangle_2) + \sum_{n=1}^2 |\psi_n^0\rangle_3 \right)
\end{aligned}$$

where the upper and lower signs respectively refer to $\alpha = x$ and y , $\lambda_x = -1$ and $\lambda_y = i$.

$$\begin{aligned}
C_{s_{1\pm,1}} &= \frac{-\sqrt{6}J_1}{(-J_1 + 3J_2 \mp d_s)}, C_{s_{1\pm,2}} = 1, C_{s_{1\pm,3}} = \frac{-\sqrt{2}(2J_2 - J_1)}{(3J_1 - J_2 \mp d_s)} \\
C_{t_{1\pm,1}^\alpha} &= \frac{2J_1(J_1 - J_2 \mp d_{t_1}) - 8J_1J_2}{8J_2^2 - (3J_1 + J_2 \mp d_{t_1})(J_1 - J_2 \mp d_{t_1})}, C_{t_{1\pm,2}^\alpha} = 1, \\
C_{t_{1\pm,3}^\alpha} &= \frac{2\sqrt{2}(2J_1J_2 - J_1(3J_1 + J_2 \mp d_{t_a}))}{(3J_1 + J_2 \mp d_{t_a})(J_1 - J_2 \mp d_{t_a}) - 8J_2^2}, \\
C_{t_{1\pm,1}^z} &= \frac{\sqrt{6}J_1(3J_1 - J_2 \mp d_{t_1})}{2(2J_2 + J_1)^2 - (3J_1 + J_2 \mp d_{t_1})(3J_1 - J_2 \mp d_{t_1})}, C_{t_{1\pm,2}^z} = 1, \\
C_{t_{1\pm,3}^z} &= \frac{-2\sqrt{3}J_1(2J_2 + J_1)}{2(2J_2 + J_1)^2 - (3J_1 + J_2 \mp d_{t_1})(3J_1 - J_2 \mp d_{t_1})}, \\
C_{t_{2\pm,1}^\alpha} &= C_{t_{3\pm,1}^\alpha} = \frac{8J_1J_2 + 2J_1(-J_1 + J_2 \mp d_{t_2})}{(3J_1 - J_2 \mp d_{t_2})(-J_1 + J_2 \mp d_{t_2}) - 8J_2^2}, C_{t_{2\pm,2}^\alpha} = C_{t_{3\pm,2}^\alpha} = 1, \\
C_{t_{2\pm,3}^\alpha} &= C_{t_{3\pm,3}^\alpha} = \frac{2\sqrt{2}(J_1(3J_1 - J_2 \mp d_{t_2}) + 2J_2J_1)}{(3J_1 - J_2 \mp d_{t_2})(-J_1 + J_2 \mp d_{t_2}) - 8J_2^2}, \\
C_{t_{2\pm,1}^z} &= C_{t_{3\pm,1}^z} = \frac{2\sqrt{2}(J_1 - J_2)}{3J_1 + J_2 \pm d_{t_2}}, C_{t_{2\pm,2}^z} = C_{t_{3\pm,2}^z} = 1, \\
\mu_{s_{1\pm}} &= \sqrt{C_{s_{1\pm,1}}^2 + C_{s_{1\pm,2}}^2 + C_{s_{1\pm,3}}^2}, \mu_{t_{1\pm}^\alpha} = \sqrt{C_{t_{1\pm,1}^\alpha}^2 + C_{t_{1\pm,2}^\alpha}^2 + C_{t_{1\pm,3}^\alpha}^2}, \\
\mu_{t_{1\pm}^z} &= \sqrt{C_{t_{1\pm,1}^z}^2 + C_{t_{1\pm,2}^z}^2 + C_{t_{1\pm,3}^z}^2}, \mu_{t_{2\pm}^z} = \mu_{t_{3\pm}^z} = \sqrt{C_{t_{2\pm,1}^z}^2 + C_{t_{2\pm,2}^z}^2}, \\
\mu_{t_{2\pm}^\alpha} &= \mu_{t_{3\pm}^\alpha} = \sqrt{C_{t_{2\pm,1}^\alpha}^2 + C_{t_{2\pm,2}^\alpha}^2 + C_{t_{2\pm,3}^\alpha}^2}.
\end{aligned}$$

Appendix B: DETAILS OF PLAQUETTE OPERATOR THEORY

The six different spin operators, S_α^n , are expressed in terms of all singlet and triplet boson operators.

$$\begin{aligned}
S_\alpha^n = & \frac{(-1)^{n-1}}{2\mu_{s_{1\pm}}\mu_{t_{1\pm}^z}} \left(C_{s_{1\pm,1}} C_{t_{1\pm,2}^z} + \frac{C_{s_{1\pm,2}} C_{t_{1\pm,1}^z}}{3} + \frac{C_{s_{1\pm,3}} C_{t_{1\pm,3}^z}}{3} \right) \left(t_{1\pm,\alpha}^\dagger s_{1\pm} + s_{1\pm}^\dagger t_{1\pm,\alpha} \right) \\
& + \frac{(-1)^{n-1} \lambda_{n,1}}{3\sqrt{2}\mu_{s_{1\pm}}\mu_{t_{2\pm}^z}} \left(C_{s_{1\pm,2}} C_{t_{2\pm,1}^z} - 2C_{s_{1\pm,3}} C_{t_{2\pm,2}^z} \right) \left(t_{2\pm,\alpha}^\dagger s_{1\pm} + s_{1\pm}^\dagger t_{2\pm,\alpha} \right) \\
& + \frac{(-1)^{n-1} \lambda_{n,3}}{2\sqrt{6}\mu_{s_{1\pm}}\mu_{t_{3\pm}^z}} \left(C_{s_{1\pm,2}} C_{t_{3\pm,1}^z} - 2C_{s_{1\pm,3}} C_{t_{3\pm,2}^z} \right) \left(t_{3\pm,\alpha}^\dagger s_{1\pm} + s_{1\pm}^\dagger t_{3\pm,\alpha} \right) \\
& + \frac{\lambda_{n,4}}{2\sqrt{2}\mu_{s_{1\pm}}} C_{s_{1\pm,2}} \left(t_{4,\alpha}^\dagger s_{1\pm} + s_{1\pm}^\dagger t_{4,\alpha} \right) - \frac{\lambda_{n,5}}{2\sqrt{6}\mu_{s_{1\pm}}} C_{s_{1\pm,2}} \left(t_{5,\alpha}^\dagger s_{1\pm} + s_{1\pm}^\dagger t_{5,\alpha} \right) \\
& + \frac{\lambda_{n,3}}{2\sqrt{2}\mu_{t_{2\pm}^z}} C_{t_{2\pm,1}^z} \left(t_{2\pm,\alpha}^\dagger s_2 + s_2^\dagger t_{2\pm,\alpha} \right) - \frac{\lambda_{n,1}}{\sqrt{6}\mu_{t_{3\pm}^z}} C_{t_{3\pm,1}^z} \left(t_{3\pm,\alpha}^\dagger s_2 + s_2^\dagger t_{3\pm,\alpha} \right) \\
& + \frac{(-1)^{n-1} \lambda_{n,5}}{6\sqrt{2}} \left(t_{4,\alpha}^\dagger s_2 + s_2^\dagger t_{4,\alpha} \right) + \frac{(-1)^{n-1} \lambda_{n,4}}{2\sqrt{6}} \left(t_{5,\alpha}^\dagger s_2 + s_2^\dagger t_{5,\alpha} \right) + \frac{(-1)^n}{6} \left(t_{6,\alpha}^\dagger s_2 + s_2^\dagger t_{6,\alpha} \right) \\
& + \frac{(-1)^{n-1} \lambda_{n,1}}{3\sqrt{3}\mu_{t_{1\pm}^z}} \left(\sqrt{2} C_{t_{1\pm,3}^z} - C_{t_{1\pm,1}^z} \right) \left(t_{1\pm,\alpha}^\dagger s_3 + s_3^\dagger t_{1\pm,\alpha} \right) + \frac{(-1)^n}{6\sqrt{3}\mu_{t_{2\pm}^z}} \left(\sqrt{2} \lambda_{n,11} C_{t_{2\pm,1}^z} - \lambda_{n,10} C_{t_{2\pm,2}^z} \right) \left(t_{2\pm,\alpha}^\dagger s_3 + s_3^\dagger t_{2\pm,\alpha} \right) \\
& + \frac{(-1)^{n-1} \lambda_{n,3}}{6\sqrt{2}\mu_{t_{3\pm}^z}} \left(C_{t_{3\pm,1}^z} - \sqrt{2} C_{t_{3\pm,2}^z} \right) \left(t_{3\pm,\alpha}^\dagger s_3 + s_3^\dagger t_{3\pm,\alpha} \right) + \frac{\lambda_{n,6}}{2\sqrt{6}} \left(t_{4,\alpha}^\dagger s_3 + s_3^\dagger t_{4,\alpha} \right) - \frac{\lambda_{n,7}}{6\sqrt{2}} \left(t_{5,\alpha}^\dagger s_3 + s_3^\dagger t_{5,\alpha} \right) \\
& + \frac{\lambda_{n,3}}{2\sqrt{3}} \left(t_{6,\alpha}^\dagger s_3 + s_3^\dagger t_{6,\alpha} \right) + \frac{\lambda_{n,3}(-1)^{n-1}}{6\mu_{t_{1\pm}^z}} \left(\sqrt{2} C_{t_{1\pm,3}^z} - C_{t_{1\pm,1}^z} \right) \left(t_{1\pm,\alpha}^\dagger s_4 + s_4^\dagger t_{1\pm,\alpha} \right) \\
& + \frac{(-1)^{n-1} \lambda_{n,3}}{6\sqrt{2}\mu_{t_{2\pm}^z}} \left(C_{t_{2\pm,1}^z} - \sqrt{2} C_{t_{2\pm,2}^z} \right) \left(t_{2\pm,\alpha}^\dagger s_4 + s_4^\dagger t_{2\pm,\alpha} \right) + \frac{(-1)^n}{2\sqrt{3}\mu_{t_{3\pm}^z}} \left(\frac{\lambda_{n,2}}{\sqrt{2}} C_{t_{3\pm,1}^z} + \lambda_{n,14} C_{t_{3\pm,2}^z} \right) \left(t_{3\pm,\alpha}^\dagger s_4 + s_4^\dagger t_{3\pm,\alpha} \right) \\
& - \frac{\lambda_{n,7}}{6\sqrt{2}} \left(t_{4,\alpha}^\dagger s_4 + s_4^\dagger t_{4,\alpha} \right) - \frac{\lambda_{n,6}}{2\sqrt{6}} \left(t_{5,\alpha}^\dagger s_4 + s_4^\dagger t_{5,\alpha} \right) - \frac{\lambda_{n,1}}{3} \left(t_{6,\alpha}^\dagger s_4 + s_4^\dagger t_{6,\alpha} \right) \\
& - \frac{i}{6\mu_{t_{1\pm}^x}\mu_{t_{1\pm}^y}} \epsilon^{\alpha\beta\gamma} \left(C_{t_{1\pm,1}^x} C_{t_{1\pm,1}^y} + C_{t_{1\pm,2}^x} C_{t_{1\pm,2}^y} + C_{t_{1\pm,3}^x} C_{t_{1\pm,3}^y} \right) \left(t_{1\pm,\beta}^\dagger t_{1\pm,\gamma} + t_{1\pm,\beta}^\dagger t_{1\pm,\gamma} \right) \\
& - \frac{i\lambda_{n,1}}{3\sqrt{2}\mu_{t_{1\pm}^x}\mu_{t_{2\pm}^z}} \epsilon^{\alpha\beta\gamma} \left(C_{t_{1\pm,1}^x} C_{t_{2\pm,1}^z} + C_{t_{1\pm,2}^x} C_{t_{2\pm,2}^z} - 2C_{t_{1\pm,3}^x} C_{t_{2\pm,3}^z} \right) \left(t_{1\pm,\beta}^\dagger t_{2\pm,\gamma} + t_{2\pm,\beta}^\dagger t_{1\pm,\gamma} \right) \\
& - \frac{i\lambda_{n,3}}{2\sqrt{6}\mu_{t_{1\pm}^x}\mu_{t_{3\pm}^z}} \epsilon^{\alpha\beta\gamma} \left(C_{t_{1\pm,1}^x} C_{t_{3\pm,1}^z} + C_{t_{1\pm,2}^x} C_{t_{3\pm,2}^z} - 2C_{t_{1\pm,3}^x} C_{t_{3\pm,3}^z} \right) \left(t_{1\pm,\beta}^\dagger t_{3\pm,\gamma} + t_{3\pm,\beta}^\dagger t_{1\pm,\gamma} \right) \\
& - \frac{i(-1)^{n-1} \lambda_{n,4}}{4\sqrt{2}\mu_{t_{1\pm}^x}} \epsilon^{\alpha\beta\gamma} \left(C_{t_{1\pm,1}^x} - C_{t_{1\pm,2}^x} \right) \left(t_{1\pm,\beta}^\dagger t_{4,\gamma} + t_{4,\beta}^\dagger t_{1\pm,\gamma} \right) \\
& - \frac{i(-1)^n \lambda_{n,5}}{4\sqrt{6}\mu_{t_{1\pm}^x}} \epsilon^{\alpha\beta\gamma} \left(C_{t_{1\pm,1}^x} - C_{t_{1\pm,2}^x} \right) \left(t_{1\pm,\beta}^\dagger t_{5,\gamma} + t_{5,\beta}^\dagger t_{1\pm,\gamma} \right) \\
& - \frac{i}{6\mu_{t_{2\pm}^x}\mu_{t_{2\pm}^z}} \epsilon^{\alpha\beta\gamma} \left(\lambda_{n,11} (C_{t_{2\pm,1}^x} C_{t_{2\pm,1}^z} + C_{t_{2\pm,2}^x} C_{t_{2\pm,2}^z}) - \lambda_{n,10} C_{t_{2\pm,3}^x} C_{t_{2\pm,3}^z} \right) \left(t_{2\pm,\beta}^\dagger t_{2\pm,\gamma} + t_{2\pm,\beta}^\dagger t_{2\pm,\gamma} \right) \\
& + \frac{i\lambda_{n,3}}{4\sqrt{3}\mu_{t_{2\pm}^x}\mu_{t_{3\pm}^z}} \epsilon^{\alpha\beta\gamma} \left(C_{t_{2\pm,1}^x} C_{t_{3\pm,1}^z} + C_{t_{2\pm,2}^x} C_{t_{3\pm,2}^z} - 2C_{t_{3\pm,3}^x} C_{t_{3\pm,3}^z} \right) \left(t_{2\pm,\beta}^\dagger t_{3\pm,\gamma} + t_{3\pm,\beta}^\dagger t_{2\pm,\gamma} \right) \\
& - \frac{i(-1)^n}{8\mu_{t_{2\pm}^z}} \epsilon^{\alpha\beta\gamma} \left(\lambda_{n,6} C_{t_{2\pm,1}^x} - \lambda_{n,12} C_{t_{2\pm,2}^x} \right) \left(t_{2\pm,\beta}^\dagger t_{4,\gamma} + t_{4,\beta}^\dagger t_{2\pm,\gamma} \right) \\
& - \frac{i(-1)^{n-1}}{8\sqrt{3}\mu_{t_{2\pm}^z}} \epsilon^{\alpha\beta\gamma} \left(\lambda_{n,7} C_{t_{2\pm,1}^x} - \lambda_{n,15} C_{t_{2\pm,2}^x} \right) \left(t_{2\pm,\beta}^\dagger t_{5,\gamma} + t_{5,\beta}^\dagger t_{2\pm,\gamma} \right) \\
& - \frac{i(-1)^{n-1} \lambda_{n,3}}{2\sqrt{2}\mu_{t_{2\pm}^z}} \epsilon^{\alpha\beta\gamma} C_{t_{2\pm,1}^x} \left(t_{6,\beta}^\dagger t_{2\pm,\gamma} + t_{2\pm,\beta}^\dagger t_{6,\gamma} \right) \\
& - \frac{i}{2\mu_{t_{3\pm}^x}\mu_{t_{3\pm}^z}} \epsilon^{\alpha\beta\gamma} \left(\frac{\lambda_{n,2}}{2} (C_{t_{3\pm,1}^x} C_{t_{3\pm,1}^z} + C_{t_{3\pm,2}^x} C_{t_{3\pm,2}^z}) + \lambda_{n,14} C_{t_{3\pm,3}^x} C_{t_{3\pm,3}^z} \right) \left(t_{3\pm,\beta}^\dagger t_{3\pm,\gamma} + t_{3\pm,\beta}^\dagger t_{3\pm,\gamma} \right) \\
& - \frac{i(-1)^{n-1}}{8\sqrt{3}\mu_{t_{3\pm}^z}} \epsilon^{\alpha\beta\gamma} \left(\lambda_{n,7} C_{t_{3\pm,1}^x} + \lambda_{n,13} C_{t_{3\pm,2}^x} \right) \left(t_{3\pm,\beta}^\dagger t_{4,\gamma} + t_{4,\beta}^\dagger t_{3\pm,\gamma} \right) \\
& - \frac{i(-1)^{n-1}}{8\mu_{t_{3\pm}^z}} \epsilon^{\alpha\beta\gamma} \left(\lambda_{n,6} C_{t_{3\pm,1}^x} + \lambda_{n,16} C_{t_{3\pm,2}^x} \right) \left(t_{3\pm,\beta}^\dagger t_{5,\gamma} + t_{5,\beta}^\dagger t_{3\pm,\gamma} \right) \\
& - \frac{i(-1)^n \lambda_{n,1}}{\sqrt{6}\mu_{t_{3\pm}^z}} \epsilon^{\alpha\beta\gamma} C_{t_{3\pm,1}^x} \left(t_{3\pm,\beta}^\dagger t_{6,\gamma} + t_{6,\beta}^\dagger t_{3\pm,\gamma} \right) - \frac{5i\lambda_{n,8}}{12} \epsilon^{\alpha\beta\gamma} t_{4,\beta}^\dagger t_{4,\gamma} + \frac{i\lambda_{n,4}}{8\sqrt{3}} \epsilon^{\alpha\beta\gamma} \left(t_{4,\beta}^\dagger t_{5,\gamma} + t_{5,\beta}^\dagger t_{4,\gamma} \right) \\
& - \frac{i\lambda_{n,5}}{12\sqrt{2}} \epsilon^{\alpha\beta\gamma} \left(t_{4,\beta}^\dagger t_{6,\gamma} + t_{6,\beta}^\dagger t_{4,\gamma} \right) - \frac{i\lambda_{n,9}}{4} \epsilon^{\alpha\beta\gamma} t_{5,\beta}^\dagger t_{5,\gamma} - \frac{i\lambda_{n,4}}{4\sqrt{6}} \epsilon^{\alpha\beta\gamma} \left(t_{5,\beta}^\dagger t_{6,\gamma} + t_{6,\beta}^\dagger t_{5,\gamma} \right) - \frac{i}{3} \epsilon^{\alpha\beta\gamma} t_{6,\beta}^\dagger t_{6,\gamma}.
\end{aligned} \tag{B1}$$

The values of $\lambda_{n,k}$ are given below, where $k = 1, 2, \dots, 19$. Here, $\alpha, \beta, \gamma = x, y, z$ and $\epsilon^{\alpha\beta\gamma}$ is the completely antisymmetric tensor with $\epsilon^{xyz} = 1$. Summation convention over repeated indices is implied.

$\lambda_{n,k}$	$n=1, 4$	$n=2, 5$	$n=3, 6$	$\lambda_{n,k}$	$n=1, 4$	$n=2, 5$	$n=3, 6$
$\lambda_{n,1}$	1	$-\frac{1}{2}$	$-\frac{1}{2}$	$\lambda_{n,9}$	1	1	2
$\lambda_{n,2}$	0	1	1	$\lambda_{n,10}$	1	-2	-2
$\lambda_{n,3}$	0	-1	1	$\lambda_{n,11}$	2	$\frac{1}{2}$	$\frac{1}{2}$
$\lambda_{n,4}$	1	-1	0	$\lambda_{n,12}$	1	2	3
$\lambda_{n,5}$	1	1	-2	$\lambda_{n,13}$	3	0	3
$\lambda_{n,6}$	1	0	-1	$\lambda_{n,14}$	1	0	0
$\lambda_{n,7}$	1	-2	1	$\lambda_{n,15}$	1	4	1
$\lambda_{n,8}$	1	1	$\frac{2}{5}$	$\lambda_{n,16}$	3	2	1

The expressions of the coefficients A_η^n , B_η^n and $D_{\eta\xi}^n$ are given below.

$$\begin{aligned}
A_1^n &= \frac{(-1)^{n-1}}{2\mu_{s_1^-} \mu_{t_1^z}} \left(C_{s_1^-,1} C_{t_1^z,2} + \frac{C_{s_1^-,2} C_{t_1^z,1}}{3} + \frac{C_{s_1^-,3} C_{t_1^z,3}}{3} \right), \\
A_2^n &= \frac{(-1)^{n-1} \lambda_{n,1}}{3\sqrt{2}\mu_{s_1^-} \mu_{t_2^z}} \left(C_{s_1^-,2} C_{t_2^z,1} - 2C_{s_1^-,3} C_{t_2^z,2} \right), \\
A_3^n &= \frac{(-1)^{n-1} \lambda_{n,3}}{2\sqrt{6}\mu_{s_1^-} \mu_{t_3^z}} \left(C_{s_1^-,2} C_{t_3^z,1} - 2C_{s_1^-,3} C_{t_3^z,2} \right), \\
B_1^n &= 0, B_2^n = \frac{\lambda_{n,3}}{2\sqrt{2}\mu_{t_2^z}} C_{t_2^z,1}, B_3^n = -\frac{\lambda_{n,1}}{\sqrt{6}\mu_{t_3^z}} C_{t_3^z,1}, D_{11}^n = \frac{1}{6}, \\
D_{22}^n &= \frac{1}{6\mu_{t_2^x}^2} \left(\lambda_{n,11} (C_{t_2^x,1} C_{t_2^x,1} + C_{t_2^x,2} C_{t_2^x,2}) - \lambda_{n,10} C_{t_2^x,3} C_{t_2^x,3} \right), \\
D_{33}^n &= \frac{1}{2\mu_{t_3^x}^2} \left(\frac{\lambda_{n,2}}{2} (C_{t_3^x,1} C_{t_3^x,1} + C_{t_3^x,2} C_{t_3^x,2}) + \lambda_{n,14} C_{t_3^x,3} C_{t_3^x,3} \right), \\
D_{12}^n &= \frac{\lambda_{n,1}}{3\sqrt{2}\mu_{t_1^x} \mu_{t_2^x}} \left(C_{t_1^x,1} C_{t_2^x,1} + C_{t_1^x,2} C_{t_2^x,2} - 2C_{t_1^x,3} C_{t_2^x,3} \right), \\
D_{13}^n &= \frac{\lambda_{n,3}}{2\sqrt{6}\mu_{t_1^x} \mu_{t_3^x}} \left(C_{t_1^x,1} C_{t_3^x,1} + C_{t_1^x,2} C_{t_3^x,2} - 2C_{t_1^x,3} C_{t_3^x,3} \right), \\
D_{23}^n &= -\frac{\lambda_{n,3}}{4\sqrt{3}\mu_{t_2^x} \mu_{t_3^x}} \left(C_{t_2^x,1} C_{t_3^x,1} + C_{t_2^x,2} C_{t_3^x,2} - 2C_{t_2^x,3} C_{t_3^x,3} \right).
\end{aligned} \tag{B2}$$

Appendix C: DETAILS OF MEAN-FIELD APPROXIMATION

Explicit forms of H_{nm} terms of Eq 9 in the momentum space are given here.

$$\begin{aligned}
H_{30} &= \frac{\epsilon^{\alpha\beta\gamma}}{\sqrt{N'}} \sum_{\mathbf{p}, \mathbf{k}, \eta, \xi, \iota} Z^{\eta\xi\iota} t_{\eta^-, \mathbf{k}-\mathbf{p}, \alpha}^\dagger t_{\xi^-, \mathbf{p}, \beta}^\dagger t_{\iota^-, \mathbf{k}, \gamma} + \text{H.c.}, \\
H_{40} &= \frac{\epsilon^{\alpha\beta\gamma} \epsilon^{\alpha\lambda\nu}}{N'} \sum_{\mathbf{p}, \mathbf{q}, \mathbf{k}, \eta, \xi, \iota, \zeta} M_{\mathbf{k}}^{\eta\xi\iota\zeta} t_{\eta^-, \mathbf{p}+\mathbf{k}, \beta}^\dagger t_{\xi^-, \mathbf{q}-\mathbf{k}, \lambda}^\dagger t_{\iota^-, \mathbf{q}, \nu} t_{\zeta^-, \mathbf{p}, \gamma}, \\
H_{21} &= \frac{1}{\sqrt{N'}} \sum_{\mathbf{p}, \mathbf{k}, \eta, \xi} \left[W_{\mathbf{p}}^{\eta\xi} t_{\eta^-, \mathbf{k}-\mathbf{p}, \alpha}^\dagger t_{\xi^-, \mathbf{p}, \beta}^\dagger s_{m, \mathbf{k}} + \text{H.c.} + W_{\mathbf{p}}^{\xi\eta} s_{m, \mathbf{k}-\mathbf{p}}^\dagger t_{\eta^-, \mathbf{p}, \alpha}^\dagger t_{\xi^-, \mathbf{k}, \alpha} + \text{H.c.} \right], \\
H_{22} &= \frac{1}{N'} \sum_{\mathbf{p}, \mathbf{q}, \mathbf{k}, \eta, \xi} \left[N_{\mathbf{k}}^{\eta\xi} s_{m, \mathbf{q}+\mathbf{k}}^\dagger s_{m, \mathbf{p}+\mathbf{k}} t_{\eta^-, \mathbf{p}, \alpha}^\dagger t_{\xi^-, \mathbf{q}, \alpha} + \frac{1}{2} N_{\mathbf{k}}^{\eta\xi} s_{m, \mathbf{q}+\mathbf{k}}^\dagger s_{m, \mathbf{p}-\mathbf{k}}^\dagger t_{\eta^-, \mathbf{p}, \alpha} t_{\xi^-, \mathbf{q}, \alpha} + \text{H.c.} \right],
\end{aligned} \tag{C1}$$

$$\begin{aligned}
Z_{\mathbf{k}}^{\eta\xi\iota} &= -i\bar{s} \sum_n \left[g_Z^{\eta\xi\iota}(n) e^{-i\mathbf{k}\cdot\mathbf{n}} + g_Z^{\xi\iota\eta}(n) e^{i\mathbf{k}\cdot\mathbf{n}} \right], \\
M_{\mathbf{k}}^{\eta\xi\iota\zeta} &= -\frac{1}{2} \sum_n \left[g_M^{\eta\xi\iota\zeta}(n) e^{i\mathbf{k}\cdot\mathbf{n}} + g_M^{\iota\zeta\eta\xi}(n) e^{-i\mathbf{k}\cdot\mathbf{n}} \right], \\
W_{\mathbf{k}}^{\eta\xi} &= \bar{s} \sum_n \left[g_W^{\eta\xi}(n) e^{-i\mathbf{k}\cdot\mathbf{n}} + g_W^{\xi\eta}(n) e^{i\mathbf{k}\cdot\mathbf{n}} \right], \\
N_{\mathbf{k}}^{\eta\xi} &= \sum_n \left[g_N^{\eta\xi}(n) e^{-i\mathbf{k}\cdot\mathbf{n}} + g_N^{\xi\eta}(n) e^{i\mathbf{k}\cdot\mathbf{n}} \right].
\end{aligned} \tag{C2}$$

The g coefficients are given by

$$\begin{aligned}
g_Z^{\eta\xi\iota}(n) &= J_1 (A_\eta^1 D_{\xi\iota}^4 \delta_{n,1} + A_\eta^2 D_{\xi\iota}^5 \delta_{n,1+2} + A_\eta^3 D_{\xi\iota}^6 \delta_{n,2}) + J_2 \left((A_\eta^1 D_{\xi\iota}^5 + A_\eta^1 D_{\xi\iota}^3 + A_\eta^2 D_{\xi\iota}^4 + A_\eta^6 D_{\xi\iota}^4) \delta_{n,1} \right. \\
&\quad \left. + (A_\eta^2 D_{\xi\iota}^6 + A_\eta^3 D_{\xi\iota}^1 + A_\eta^3 D_{\xi\iota}^5 + A_\eta^4 D_{\xi\iota}^6) \delta_{n,2} + (A_\eta^1 D_{\xi\iota}^5 + A_\eta^2 D_{\xi\iota}^6 + A_\eta^2 D_{\xi\iota}^4 + A_\eta^3 D_{\xi\iota}^5) \delta_{n,1+2} \right), \\
g_Z^{\eta\xi\iota}(n) &= J_1 (D_{\eta\xi}^1 A_\iota^4 \delta_{n,1} + D_{\eta\xi}^2 A_\iota^5 \delta_{n,1+2} + D_{\eta\xi}^3 A_\iota^6 \delta_{n,2}) + J_2 \left((D_{\eta\xi}^1 A_\iota^5 + D_{\eta\xi}^1 A_\iota^3 + D_{\eta\xi}^2 A_\iota^4 + D_{\eta\xi}^6 A_\iota^4) \delta_{n,1} \right. \\
&\quad \left. + (D_{\eta\xi}^2 A_\iota^6 + D_{\eta\xi}^3 A_\iota^1 + D_{\eta\xi}^3 A_\iota^5 + D_{\eta\xi}^4 A_\iota^6) \delta_{n,2} + (D_{\eta\xi}^1 A_\iota^5 + D_{\eta\xi}^2 A_\iota^6 + D_{\eta\xi}^2 A_\iota^4 + D_{\eta\xi}^3 A_\iota^5) \delta_{n,1+2} \right), \\
g_M^{\eta\xi\iota\zeta}(n) &= J_1 (D_{\eta\xi}^1 D_{\iota\zeta}^4 \delta_{n,1} + D_{\eta\xi}^2 D_{\iota\zeta}^5 \delta_{n,1+2} + D_{\eta\xi}^3 D_{\iota\zeta}^6 \delta_{n,2}) + J_2 \left((D_{\eta\xi}^1 D_{\iota\zeta}^5 + D_{\eta\xi}^1 D_{\iota\zeta}^3 + D_{\eta\xi}^2 D_{\iota\zeta}^4 + D_{\eta\xi}^6 D_{\iota\zeta}^4) \delta_{n,1} \right. \\
&\quad \left. + (D_{\eta\xi}^2 D_{\iota\zeta}^6 + D_{\eta\xi}^3 D_{\iota\zeta}^1 + D_{\eta\xi}^3 D_{\iota\zeta}^5 + D_{\eta\xi}^4 D_{\iota\zeta}^6) \delta_{n,2} + (D_{\eta\xi}^1 D_{\iota\zeta}^5 + D_{\eta\xi}^2 D_{\iota\zeta}^6 + D_{\eta\xi}^2 D_{\iota\zeta}^4 + D_{\eta\xi}^3 D_{\iota\zeta}^5) \delta_{n,1+2} \right), \\
g_W^{\eta\xi}(n) &= J_1 (B_\eta^1 A_\xi^4 \delta_{n,1} + B_\eta^2 A_\xi^5 \delta_{n,1+2} + B_\eta^3 A_\xi^6 \delta_{n,2}) + J_2 \left((B_\eta^1 A_\xi^5 + B_\eta^1 A_\xi^3 + B_\eta^2 A_\xi^4 + B_\eta^6 A_\xi^4) \delta_{n,1} \right. \\
&\quad \left. + (B_\eta^2 A_\xi^6 + B_\eta^3 A_\xi^1 + B_\eta^3 A_\xi^5 + B_\eta^4 A_\xi^6) \delta_{n,2} + (B_\eta^1 A_\xi^5 + B_\eta^2 A_\xi^6 + B_\eta^2 A_\xi^4 + B_\eta^3 A_\xi^5) \delta_{n,1+2} \right), \\
g_W^{\eta\xi}(n) &= J_1 (A_\eta^1 B_\xi^4 \delta_{n,1} + A_\eta^2 B_\xi^5 \delta_{n,1+2} + A_\eta^3 B_\xi^6 \delta_{n,2}) + J_2 \left((A_\eta^1 B_\xi^5 + A_\eta^1 B_\xi^3 + A_\eta^2 B_\xi^4 + A_\eta^6 B_\xi^4) \delta_{n,1} \right. \\
&\quad \left. + (A_\eta^2 B_\xi^6 + A_\eta^3 B_\xi^1 + A_\eta^3 B_\xi^5 + A_\eta^4 B_\xi^6) \delta_{n,2} + (A_\eta^1 B_\xi^5 + A_\eta^2 B_\xi^6 + A_\eta^2 B_\xi^4 + A_\eta^3 B_\xi^5) \delta_{n,1+2} \right), \\
g_N^{\eta\xi}(n) &= J_1 (B_\eta^1 B_\xi^4 \delta_{n,1} + B_\eta^2 B_\xi^5 \delta_{n,1+2} + B_\eta^3 B_\xi^6 \delta_{n,2}) + J_2 \left((B_\eta^1 B_\xi^5 + B_\eta^1 B_\xi^3 + B_\eta^2 B_\xi^4 + B_\eta^6 B_\xi^4) \delta_{n,1} \right. \\
&\quad \left. + (B_\eta^2 B_\xi^6 + B_\eta^3 B_\xi^1 + B_\eta^3 B_\xi^5 + B_\eta^4 B_\xi^6) \delta_{n,2} + (B_\eta^1 B_\xi^5 + B_\eta^2 B_\xi^6 + B_\eta^2 B_\xi^4 + B_\eta^3 B_\xi^5) \delta_{n,1+2} \right).
\end{aligned} \tag{C3}$$

Here, $\eta, \xi, \iota, \zeta = 1, 2, 3$ and $\alpha, \beta, \gamma = x, y, z$. $m = 2$ and 1^- for the regions R_1 and R_2 , respectively. The coefficients, $X_{\mathbf{k}}^{\eta\xi}$ and $Y_{\mathbf{k}}^{\eta\xi}$ are given as

$$\begin{aligned}
X_{\mathbf{k}}^{\eta\xi} &= (E_{t_\eta} - \mu) (\delta_{\eta,1^-} \delta_{\xi,1^-} + \delta_{\eta,2^-} \delta_{\xi,2^-} + \delta_{\eta,3^-} \delta_{\xi,3^-}) + Y_{\mathbf{k}}^{\eta\xi}, \\
Y_{\mathbf{k}}^{\eta\xi} &= \bar{s}^2 \sum_n 2g^{\eta\xi}(n) \cos(\mathbf{k} \cdot \mathbf{n}), \quad \text{where} \\
g^{\eta\xi}(n) &= J_1 (A_\eta^1 A_\xi^4 \delta_{n,1} + A_\eta^2 A_\xi^5 \delta_{n,1+2} + A_\eta^3 A_\xi^6 \delta_{n,2}) + J_2 \left((A_\eta^1 A_\xi^5 + A_\eta^1 A_\xi^3 + A_\eta^2 A_\xi^4 + A_\eta^6 A_\xi^4) \delta_{n,1} \right. \\
&\quad \left. + (A_\eta^2 A_\xi^6 + A_\eta^3 A_\xi^1 + A_\eta^3 A_\xi^5 + A_\eta^4 A_\xi^6) \delta_{n,2} + (A_\eta^1 A_\xi^5 + A_\eta^2 A_\xi^6 + A_\eta^2 A_\xi^4 + A_\eta^3 A_\xi^5) \delta_{n,1+2} \right).
\end{aligned} \tag{C4}$$

Here, $\eta, \xi = 1, 2, 3$ and E_{t_η} is the triplet energy of the single plaquette. $n = 1, 2$ correspond to the NN vectors $\boldsymbol{\tau}_1$ and $\boldsymbol{\tau}_2$. The expressions of all g coefficients in the region R_2 will be same with the interchange of A and B .

The analytic procedure used to diagonalize the mean-field Hamiltonian (Eq 15) expressed in terms of bosonic operators has been described below. Instead of $H_{\mathbf{k}}$, $I_B H_{\mathbf{k}}$ has been diagonalized³⁵, where $I_B = \text{diag}[1, 1, 1, -1, -1, -1]$.

The characteristic equation and positive eigenvalues of the matrix $I_B H_{\mathbf{k}}$ are written below.

$$\begin{aligned} \Omega_{\mathbf{k}}^6 + a_{2,\mathbf{k}}\Omega_{\mathbf{k}}^4 + a_{1,\mathbf{k}}\Omega_{\mathbf{k}}^2 + a_{0,\mathbf{k}} &= 0, \\ \Omega_{\eta,\mathbf{k}} &= \left[2\sqrt{-Q_{\mathbf{k}}}\cos\left(\frac{\theta}{3} - \frac{2\pi p}{3}\right) - \frac{a_{2,\mathbf{k}}}{3} \right]^{\frac{1}{2}}, \quad Q_{\mathbf{k}} = \frac{3a_{1,\mathbf{k}} - a_{1,\mathbf{k}}^2}{9}, \\ R_{\mathbf{k}} &= \frac{9a_{2,\mathbf{k}}a_{1,\mathbf{k}} - 27a_{0,\mathbf{k}} - 2a_{1,\mathbf{k}}^3}{54}, \quad \cos(\theta) = \frac{-R_{\mathbf{k}}}{Q_{\mathbf{k}}\sqrt{-Q_{\mathbf{k}}}}, \end{aligned} \quad (\text{C5})$$

where, $p = 0, 1, 2$ and $\eta = 1, 2, 3$. The coefficients, $a_{i,\mathbf{k}}$ are given below.

$$\begin{aligned} a_{2,\mathbf{k}} &= -(w_{11,\mathbf{k}}^2 + w_{22,\mathbf{k}}^2 + w_{33,\mathbf{k}}^2), \\ a_{1,\mathbf{k}} &= w_{11,\mathbf{k}}^2 w_{22,\mathbf{k}}^2 + w_{11,\mathbf{k}}^2 w_{33,\mathbf{k}}^2 + w_{22,\mathbf{k}}^2 w_{33,\mathbf{k}}^2 - 4(Y_{\mathbf{k}}^{12})^2 (X_{\mathbf{k}}^{11} - Y_{\mathbf{k}}^{11}) (X_{\mathbf{k}}^{22} - Y_{\mathbf{k}}^{22}) \\ &\quad - 4(Y_{\mathbf{k}}^{23})^2 (X_{\mathbf{k}}^{22} - Y_{\mathbf{k}}^{22}) (X_{\mathbf{k}}^{33} - Y_{\mathbf{k}}^{33}) - 4(Y_{\mathbf{k}}^{13})^2 (X_{\mathbf{k}}^{11} - Y_{\mathbf{k}}^{11}) (X_{\mathbf{k}}^{33} - Y_{\mathbf{k}}^{33}), \\ a_{0,\mathbf{k}} &= (X_{\mathbf{k}}^{11} - Y_{\mathbf{k}}^{11}) (X_{\mathbf{k}}^{22} - Y_{\mathbf{k}}^{22}) (X_{\mathbf{k}}^{33} - Y_{\mathbf{k}}^{33}) [4(Y_{\mathbf{k}}^{12})^2 (X_{\mathbf{k}}^{33} + Y_{\mathbf{k}}^{33}) + 4(Y_{\mathbf{k}}^{23})^2 (X_{\mathbf{k}}^{11} + Y_{\mathbf{k}}^{11}) \\ &\quad + 4(Y_{\mathbf{k}}^{13})^2 (X_{\mathbf{k}}^{22} + Y_{\mathbf{k}}^{22}) - 16Y_{\mathbf{k}}^{12}Y_{\mathbf{k}}^{13}Y_{\mathbf{k}}^{23} - (X_{\mathbf{k}}^{11} + Y_{\mathbf{k}}^{11}) (X_{\mathbf{k}}^{22} + Y_{\mathbf{k}}^{22}) (X_{\mathbf{k}}^{33} + Y_{\mathbf{k}}^{33})], \end{aligned} \quad (\text{C6})$$

where, $w_{\eta\xi,\mathbf{k}}^2 = (X_{\mathbf{k}}^{\eta\xi})^2 - (Y_{\mathbf{k}}^{\eta\xi})^2$ with $\eta, \xi = 1, 2, 3$.

Using the procedure developed before³⁵, analytic expressions of the Bogoliubov coefficients have been obtained. The Bogoliubov coefficients $u_{\mathbf{k}}^{\eta\xi}$ and $v_{\mathbf{k}}^{\eta\xi}$ are

$$u_{\mathbf{k}}^{\eta\xi} = \frac{\phi_{\mathbf{k}}^{\eta\xi} + \psi_{\mathbf{k}}^{\eta\xi}}{2}, \quad v_{\mathbf{k}}^{\eta\xi} = \frac{\phi_{\mathbf{k}}^{\eta\xi} - \psi_{\mathbf{k}}^{\eta\xi}}{2}, \quad (\text{C7})$$

with $\eta, \xi = 1, 2$ and 3. Where,

$$\begin{aligned} \phi_{\mathbf{k}}^{1\eta} &= x_{\eta,\mathbf{k}}\sqrt{X_{\mathbf{k}}^{11} - Y_{\mathbf{k}}^{11}}, \quad \phi_{\mathbf{k}}^{2\eta} = y_{\eta,\mathbf{k}}\sqrt{X_{\mathbf{k}}^{22} - Y_{\mathbf{k}}^{22}}, \quad \phi_{\mathbf{k}}^{3\eta} = z_{\eta,\mathbf{k}}\sqrt{X_{\mathbf{k}}^{33} - Y_{\mathbf{k}}^{33}}, \\ \psi_{\mathbf{k}}^{1\eta} &= (x_{\eta,\mathbf{k}}(X_{\mathbf{k}}^{11} + Y_{\mathbf{k}}^{11})\sqrt{X_{\mathbf{k}}^{11} - Y_{\mathbf{k}}^{11}} + 2y_{\eta,\mathbf{k}}Y_{\mathbf{k}}^{12}\sqrt{X_{\mathbf{k}}^{22} - Y_{\mathbf{k}}^{22}} + 2z_{\eta,\mathbf{k}}Y_{\mathbf{k}}^{13}\sqrt{X_{\mathbf{k}}^{33} - Y_{\mathbf{k}}^{33}})/\Omega_{\eta,\mathbf{k}}, \\ \psi_{\mathbf{k}}^{2\eta} &= (2x_{\eta,\mathbf{k}}Y_{\mathbf{k}}^{12}\sqrt{X_{\mathbf{k}}^{11} - Y_{\mathbf{k}}^{11}} + y_{\eta,\mathbf{k}}(X_{\mathbf{k}}^{22} + Y_{\mathbf{k}}^{22})\sqrt{X_{\mathbf{k}}^{22} - Y_{\mathbf{k}}^{22}} + 2z_{\eta,\mathbf{k}}Y_{\mathbf{k}}^{23}\sqrt{X_{\mathbf{k}}^{33} - Y_{\mathbf{k}}^{33}})/\Omega_{\eta,\mathbf{k}}, \\ \psi_{\mathbf{k}}^{3\eta} &= (2x_{\eta,\mathbf{k}}Y_{\mathbf{k}}^{13}\sqrt{X_{\mathbf{k}}^{11} - Y_{\mathbf{k}}^{11}} + 2y_{\eta,\mathbf{k}}Y_{\mathbf{k}}^{23}\sqrt{X_{\mathbf{k}}^{22} - Y_{\mathbf{k}}^{22}} + z_{\eta,\mathbf{k}}(X_{\mathbf{k}}^{33} + Y_{\mathbf{k}}^{33})\sqrt{X_{\mathbf{k}}^{33} - Y_{\mathbf{k}}^{33}})/\Omega_{\eta,\mathbf{k}}, \\ x_{\eta,\mathbf{k}} &= \frac{M_{\eta,\mathbf{k}}}{\sqrt{G_{\eta,\mathbf{k}}}}, \quad y_{\eta,\mathbf{k}} = \frac{1}{\sqrt{G_{\eta,\mathbf{k}}}}, \quad z_{\eta,\mathbf{k}} = \frac{N_{\eta,\mathbf{k}}}{\sqrt{G_{\eta,\mathbf{k}}}}, \quad M_{\eta,\mathbf{k}} = \frac{A_{\mathbf{k}}C_{\mathbf{k}} - (w_{22,\mathbf{k}}^2 - \Omega_{\eta,\mathbf{k}}^2)B_{\mathbf{k}}}{A_{\mathbf{k}}B_{\mathbf{k}} - (w_{11,\mathbf{k}}^2 - \Omega_{\eta,\mathbf{k}}^2)C_{\mathbf{k}}}, \\ N_{\eta,\mathbf{k}} &= \frac{C_{\mathbf{k}} + B_{\mathbf{k}}M_{\eta,\mathbf{k}}}{(\Omega_{\eta,\mathbf{k}}^2 - w_{33,\mathbf{k}}^2)}, \quad G_{\eta,\mathbf{k}} = \Omega_{\eta,\mathbf{k}} [1 + M_{\eta,\mathbf{k}}^2 + N_{\eta,\mathbf{k}}^2], \\ A_{\mathbf{k}} &= 2Y_{\mathbf{k}}^{12}\sqrt{X_{\mathbf{k}}^{11} - Y_{\mathbf{k}}^{11}}\sqrt{X_{\mathbf{k}}^{22} - Y_{\mathbf{k}}^{22}}, \\ B_{\mathbf{k}} &= 2Y_{\mathbf{k}}^{13}\sqrt{X_{\mathbf{k}}^{11} - Y_{\mathbf{k}}^{11}}\sqrt{X_{\mathbf{k}}^{33} - Y_{\mathbf{k}}^{33}}, \\ C_{\mathbf{k}} &= 2Y_{\mathbf{k}}^{23}\sqrt{X_{\mathbf{k}}^{22} - Y_{\mathbf{k}}^{22}}\sqrt{X_{\mathbf{k}}^{33} - Y_{\mathbf{k}}^{33}}. \end{aligned} \quad (\text{C8})$$